Cancer Cell

Article

In vivo macrophage engineering reshapes the tumor microenvironment leading to eradication of liver metastases

Graphical abstract

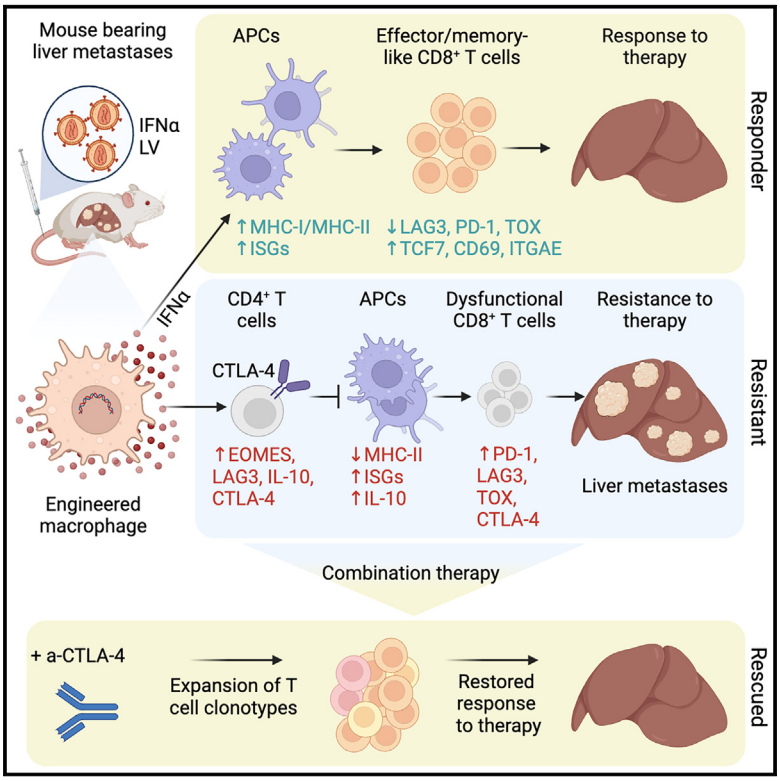

Highlights

- IFNα from *in vivo* LV-engineered liver macrophages curbs liver metastasis growth
- IFNα activates antigen presentation and CD8⁺ T cell effector function
- Resistance to IFNα is associated with *Eomes* CD4⁺ T cells, IL-10 signaling, and CTLA-4
- IFNα combined with anti-CTLA-4 bypasses resistance attaining complete response

Authors

Thomas Kerzel, Giovanna Giacca, Stefano Beretta, ..., Francesca Sanvito, Luigi Naldini, Mario Leonardo Squadrito

Correspondence

naldini.luigi@hsr.it (L.N.), squadrito.mario@hsr.it (M.L.S.)

In brief

In this study, Kerzel et al. describe a lentiviral vector platform to selectively engineer liver macrophages to deliver IFNα to liver metastases from within the tissue achieving therapeutic efficacy. Simultaneous combination with anti-CTLA-4 bypassed resistance mechanisms and expanded tumor-reactive T cells, attaining complete response in most mice.

Kerzel et al., 2023, Cancer Cell *41*, 1892–1910
November 13, 2023
https://doi.org/10.1016/j.ccell.2023.09.014

CellPress

CellPress
OPEN ACCESS

Cancer Cell

Article

In vivo macrophage engineering reshapes the tumor microenvironment leading to eradication of liver metastases

Thomas Kerzel,[1,2,16] Giovanna Giacca,[1,2,16] Stefano Beretta,[1,3] Chiara Bresesti,[1,2] Marco Notaro,[1,2] Giulia Maria Scotti,[4] Chiara Balestrieri,[4,5] Tamara Canu,[6] Miriam Redegalli,[7] Federica Pedica,[2,7] Marco Genua,[8] Renato Ostuni,[2,8] Anna Kajaste-Rudnitski,[9] Masanobu Oshima,[10] Giovanni Tonon,[2,4] Ivan Merelli,[3,11] Luca Aldrighetti,[2,12] Paolo Dellabona,[13] Nadia Coltella,[1] Claudio Doglioni,[2,7] Paola M.V. Rancoita,[14] Francesca Sanvito,[7,15] Luigi Naldini,[1,2,17,*] and Mario Leonardo Squadrito[1,2,17,18,*]

[1]Targeted Cancer Gene Therapy Unit, San Raffaele Telethon Institute for Gene Therapy, IRCCS San Raffaele Scientific Institute, 20132 Milan, Italy
[2]Vita Salute San Raffaele University, 20132 Milan, Italy
[3]Bioinformatics Core, San Raffaele Telethon Institute for Gene Therapy, IRCCS San Raffaele Scientific Institute, 20132 Milan, Italy
[4]Center for Omics Sciences, IRCCS San Raffaele Scientific Institute, 20132 Milan, Italy
[5]Experimental Hematology Unit, IRCCS San Raffaele Scientific Institute, 20132 Milan, Italy
[6]Preclinical Imaging Facility, IRCCS San Raffaele Scientific Institute, 20132 Milan, Italy
[7]Pathology Unit, IRCCS San Raffaele Scientific Institute, 20132 Milan, Italy
[8]Genomics of the Innate Immune System Unit, San Raffaele Telethon Institute for Gene Therapy, IRCCS San Raffaele Scientific Institute, 20132 Milan, Italy
[9]Retrovirus-Host Interactions and Innate Immunity to Gene Transfer, San Raffaele Telethon Institute for Gene Therapy, IRCCS San Raffaele Scientific Institute, 20132 Milan, Italy
[10]Division of Genetics, Cancer Research Institute, Kanazawa University, Kanazawa 920-1192, Japan
[11]National Research Council, Institute for Biomedical Technologies, 20054 Segrate, Italy
[12]Hepatobiliary Surgery Division, IRCCS San Raffaele Scientific Institute, 20132 Milan, Italy
[13]Division of Immunology, Transplantation and Infectious Diseases, IRCCS San Raffaele Scientific Institute, 20132 Milan, Italy
[14]CUSSB University Center for Statistics in the Biomedical Science, Vita Salute San Raffaele University, 20132 Milan, Italy
[15]GLP Test Facility, San Raffaele Telethon Institute for Gene Therapy, IRCCS San Raffaele Scientific Institute, 20132 Milan, Italy
[16]These authors contributed equally
[17]Senior author
[18]Lead contact
*Correspondence: naldini.luigi@hsr.it (L.N.), squadrito.mario@hsr.it (M.L.S.)
https://doi.org/10.1016/j.ccell.2023.09.014

SUMMARY

Liver metastases are associated with poor response to current pharmacological treatments, including immunotherapy. We describe a lentiviral vector (LV) platform to selectively engineer liver macrophages, including Kupffer cells and tumor-associated macrophages (TAMs), to deliver type I interferon (IFNα) to liver metastases. Gene-based IFNα delivery delays the growth of colorectal and pancreatic ductal adenocarcinoma liver metastases in mice. Response to IFNα is associated with TAM immune activation, enhanced MHC-II-restricted antigen presentation and reduced exhaustion of $CD8^+$ T cells. Conversely, increased IL-10 signaling, expansion of *Eomes* $CD4^+$ T cells, a cell type displaying features of type I regulatory T (Tr1) cells, and CTLA-4 expression are associated with resistance to therapy. Targeting regulatory T cell functions by combinatorial CTLA-4 immune checkpoint blockade and IFNα LV delivery expands tumor-reactive T cells, attaining complete response in most mice. These findings support a promising therapeutic strategy with feasible translation to patients with unmet medical need.

INTRODUCTION

The presence of liver metastases of gastrointestinal tumors, such as colorectal cancer (CRC) and pancreatic ductal adenocarcinoma (PDAC), is a negative prognostic factor for patients with cancer. Despite the progress in pharmacological treatments, such as immunotherapeutic and tumor-targeted approaches, the most effective treatment option remains surgical resection, which is applicable to a limited number of patients and often with partial success.[1] The high incidence of liver metastases is in part attributed to the blood flow from the digestive system toward the liver and the architecture and functional features of hepatic sinusoids,

which together favor metastatic colonization, as well as the tolerogenic microenvironment of the liver, which inhibits protective immune responses.[2,3] The tumor microenvironment (TME) of liver metastases suppresses immunity by a plethora of mechanisms including presence of pro-tumoral macrophages and other myeloid lineage cells. Moreover, high levels of immunosuppressive molecules such as interleukin 10 (IL-10) reduce antigen presentation by professional antigen-presenting cells (APCs)[4] leading to accumulation of immunosuppressive cell populations such as regulatory $CD4^+$ T cells (Tregs)[5,6] and type-1-like regulatory (Tr1) T cells,[7] which together dampen the therapeutic efficacy of current cancer immunotherapies, such as immune checkpoint inhibitors.[8] Indeed, liver metastases originating from microsatellite stable CRC, which represent most CRC cases, poorly respond to conventional cancer immunotherapy.[9] Moreover, the presence of liver metastases impairs the response to immune checkpoint inhibitors of distinct cancer types, e.g., melanoma, which normally responds to this therapy.[8,10]

Enforcing cytokine expression in the liver through genetic engineering of liver macrophages, including Kupffer cells (KCs) and tumor-associated macrophages (TAMs), may provide an effective strategy to reprogram the liver TME toward an immune reactive state, enabling development of protective antitumoral immune responses.[11] Interferon α (IFNα) is a cytokine known for its antiviral and pleiotropic immune activities and may be a potential candidate to reprogram the liver TME by concomitantly enhancing anti-tumoral functions of immune cells while targeting neo-angiogenic endothelial cells and cancer cells.[12] However, its clinical use as systemically delivered drug has been hampered by severe off-tumor side effects and unfavorable pharmacodynamics and pharmacokinetics.[13,14]

Biodistribution studies in mice and non-human primates have shown that vesicular-stomatitis-virus glycoprotein (VSV-G) pseudotyped lentiviral vectors (hereon LVs) target preferentially the liver and spleen upon systemic administration.[15,16] Liver gene transfer is favored by specific functional and anatomic features of the hepatic micro-vasculature and is mediated by high expression of the low-density lipoprotein receptor in hepatocytes, which serves as entry receptor for LVs, as well as active uptake by liver phagocytic cells.[17,18] Among phagocytic cells in the liver, resident macrophages, termed Kupffer cells (KCs), are highly targeted by LVs[15] and due to their anatomical localization, lining the sinusoids, and the potential to infiltrate the tumor may constitute a suitable cellular platform for selective delivery of IFNα to tumors in the liver.

Here, we describe a liver macrophage-directed gene transfer strategy that upon a single well-tolerated intravenous infusion of an IFNα-expressing LV rapidly promotes a therapeutic response against diverse mouse models of CRC and PDAC liver metastases by enabling innate and adaptive immune activation. Overall, our study sets the ground for clinical development of a gene therapy strategy with the potential to address the current unmet medical need of patients affected by liver metastases.

RESULTS

Generation of an LV platform enabling *in vivo* liver macrophage engineering

We first generated LVs containing a putative 1.8 kb promoter sequence obtained from the mouse mannose receptor C-type 1 *(Mrc1)* gene (Figure S1A). MRC1 is expressed by most macrophage subsets, including KCs, and is upregulated by alternatively activated macrophages, such as TAMs.[19] We then cloned a GFP coding sequence downstream of the *Mrc1* promoter sequence (originating the *Mrc1*.GFP LV) and produced *Mrc1*.GFP LV stocks (Figure 1A). *Mrc1*.GFP LV drove robust transgene expression in IL-4-exposed (M2-like) bone marrow-derived macrophages (BMDMs) but not in LPS/IFNγ-exposed (M1-like) BMDMs (Figures S1B–S1E). Intravenous injection (i.v.) of *Mrc1*.GFP LV to immunocompromized mice resulted in GFP expression selectively in liver cells (KCs and liver sinusoidal endothelial cells, LSECs) and in some splenic cells (*Mrc1*-positive macrophages). We did not observe GFP expression or integrated LV copies in blood cells, bone marrow, or other organs such as the lung, subiliac lymph nodes, small intestine, and brain (Figures 1B–1D). To further fine-tune gene expression to macrophages, we leveraged on endogenous microRNA (miRNA) regulation, which was exploited to abate the expression of the transgene in off-target cells by incorporating complementary miRNA target sequences (miRTs) at its 3′ UTR. In a bidirectional vector design, four tandem copies of miRT-122-5p fully prevented GFP expression in hepatocytes while preserving it in KCs, whereas 4 copies of miRT-126-3p prevented GFP expression in LSECs but not in KCs (Figures S1F–S1K). Building on these results, we incorporated 4 copies each of miRT-122-5p and miRT-126-3p downstream of GFP in the *Mrc1*.GFP LV generating the *Mrc1*.GFP.miRT LV (Figure 1A). We then implanted either mCherry-expressing MC38 CRC cells via intrahepatic injection, or CRC cells derived from $APC^{\Delta 716}$; $Kras^{G12D}$; $Tgfbr2^{-/-}$; $Trp53^{R270H}$; $Fbxw7^{-/-}$ mice, hereon referred as AKTPF CRC cells,[20] via intrasplenic injection to better recapitulate multifocal metastatic seeding to the liver. We injected i.v. the *Mrc1*.GFP or the *Mrc1*.GFP.miRT LV to mice challenged with liver metastases. In agreement with our findings in tumor-free mice, the *Mrc1*.GFP drove GFP expression in liver macrophages, LSECs, and splenic MRC1-positive macrophages, whereas in the presence of miRNA regulation (*Mrc1*.GFP.miRT LV), GFP expression in LSECs was virtually completely abated (Figure 1E). In both MC38- and AKTPF-derived metastatic lesions, we found enrichment for GFP^+ cells in liver peri-metastatic areas, in particular in $F4/80^+VSIG4^+$ and $F4/80^+CLEC4F^+$ KCs, indicating preferential transduction and/or upregulation of *Mrc1* promoter activity in KCs of this area. Of note, there was also a small fraction of GFP^+ cells among the $F4/80^+$ $CLEC4F^-$ or $F4/80^+$ $VSIG4^-$ macrophages, which were predominant within the tumor and likely represented monocyte-derived TAMs (Figures 1F, 1G, S1L, and S1M). We did not observe GFP expression in other organs such as the brain, small intestine, lung, and subiliac lymph nodes (Figure S1N). In summary, the selective biodistribution and expression in liver macrophages of the newly developed *Mrc1*.GFP.miRT LV, together with its enriched expression in areas surrounding tumor lesions, supports the feasibility of *in vivo* genetically engineering liver macrophages (including KCs and TAMs) for delivery of therapeutic molecules to liver metastatic lesions.

In vivo LV-engineered liver macrophages enable rapid, sustained and well-tolerated IFNα production

We then exploited engineered macrophages to deliver IFNα to liver metastases. To this aim, we replaced the GFP with an

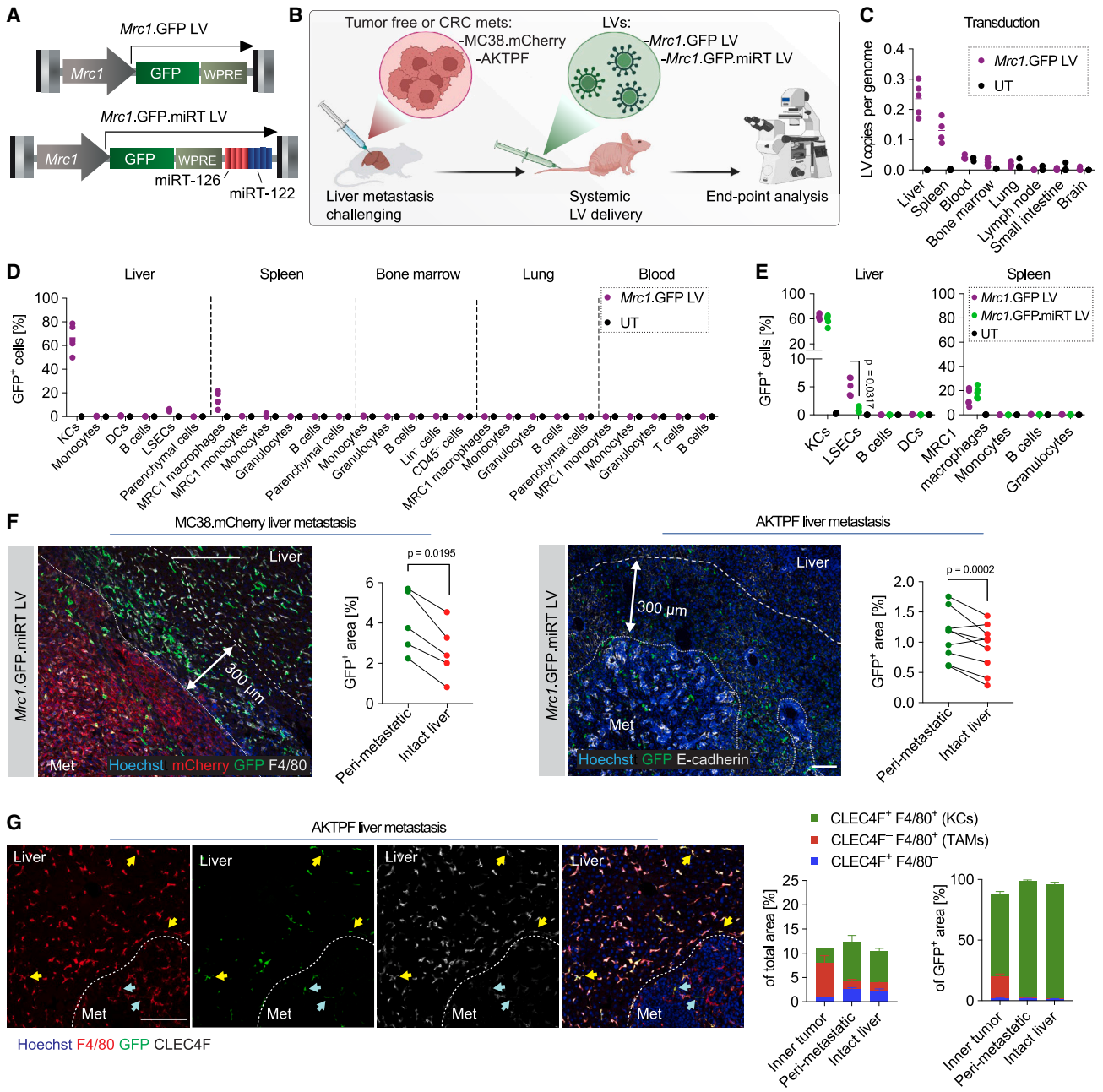

Figure 1. Generation of an LV platform enabling *in vivo* liver macrophage engineering

(A) Schematics of *Mrc1*.GFP and *Mrc1*.GFP.miRT LVs.

(B) Schematics of the experiments shown in panels C-G.

(C–E) Biodistribution analysis of *Mrc1*.GFP and *Mrc1*.GFP.miRT LVs. In C, LV copies per genome of the indicated organs by digital droplet PCR (ddPCR) analysis (horizontal lines represents Mean). In D and E, GFP expression in the indicated cell types in the indicated organs by flow cytometry (FC) analysis. (n = 5 mice/group, statistical analysis by Mann-Whitney test comparing only *Mrc1*.GFP LV vs. *Mrc1*.GFP.miRT LV and p values adjusted for multiple testing with Bonferroni's correction). In E, *Mrc1*.GFP LV and *Mrc1*.GFP.miRT LV were used at $3*10^{10}$ TU/kg.

(F and G) Biodistribution of the *Mrc1*.GFP.miRT LV in livers bearing CRC liver metastases. In F, representative immunofluorescence (IF) images obtained by confocal microscopy (CM) and relative GFP quantification of livers bearing metastases from MC38.mCherry cells in the left panel, mCherry (red), GFP (green), F4/80 (gray), and nuclei (blue, left panel), scale bar 200 µm or AKTPF CRC cells in right panel, GFP (green), F4/80 (gray) and nuclei (blue, right panel); metastasis (Met), peri-metastatic area (dotted line) and intact liver are indicated, scale bar 100 µm. In the left panel, MC38 cells were injected 10 days after LV delivery, LV at $3*10^{10}$ TU/kg; in the right panel, *Mrc1*.GFP.miRT LV was used at $5*10^{9}$ TU/kg in NSG mice (n = 5 mice/group; statistical analysis by bootstrap t test). In G, representative IF image and relative quantification of GFP^+ cells and macrophage populations within livers bearing AKTPF CRC metastases, *Mrc1*.GFP.miRT LV injected at day 5 after tumor implantation at $1.5*10^{10}$ TU/mouse. F4/80 (red), GFP (green), CLEC4F (gray), and nuclei (blue, left panel) metastasis (Met), KCs (yellow arrows), and TAMs (light blue arrows) are indicated (n = 5 mice/group, Mean +SEM); scale bar 150 µm.

See also Figure S1.

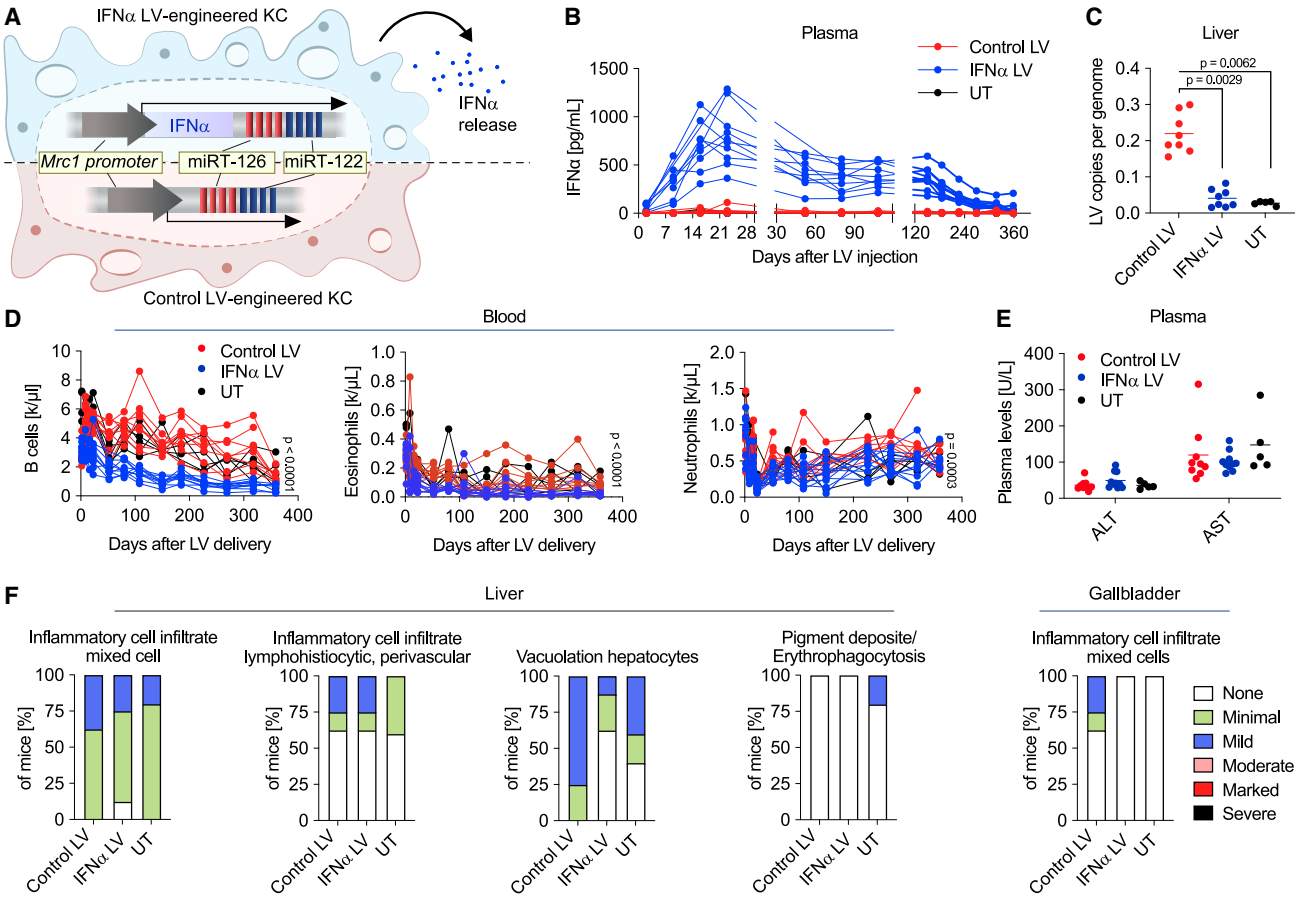

Figure 2. *In vivo* LV-engineered liver macrophages enable rapid, sustained, and well-tolerated IFNα production

(A) Schematics of a KC engineered with the IFNα LV (top) or the Control LV (bottom).

(B) Plasma IFNα levels by ELISA analysis at the indicated time points upon LV injection at $5*10^9$ TU/kg (n = 10, 10, 5 mice/group in Control LV, IFNα LV, or untransduced, UT, respectively).

(C) LV copies per genome by ddPCR analysis at endpoint, day 366 after LV injection. (n = 8, 8, 5 mice/group; horizontal line represents Mean, statistical analysis by Kruskal-Wallis with Dunn's tests, adjusted p value by Bonferroni's correction).

(D) Blood cell counts of B cells (left panel), eosinophils (middle panel), and neutrophils (right panel) at the indicated time points upon LV injection (n values as in B; statistical analysis by Mann-Whitney test on area under the curve values).

(E) Plasma levels of alanine transaminase (ALT) and aspartate aminotransferase (AST) at 126 days after LV injection (n = 9, 10, 5 mice/group, horizontal line represents Mean, statistical analysis by Kruskal-Wallis test).

(F) Histopathologic analysis of the indicated organs at day 366 upon LV injection (n values as in C).

See also Figure S2.

IFNα-coding DNA sequence in the *Mrc1*.GFP.miRT LV, originating the hereon termed IFNα LV. In order to efficiently transduce liver macrophages, we produced LVs based on a manufacturing process (described previously[21]) aimed to yield high-titer LV stocks with low levels of contaminants, such as plasmids and endotoxin, which could lead to bystander innate immune activation or adverse systemic effects. We then engineered liver macrophages *in vivo* by injecting i.v. either the IFNα LV or an LV with the same regulatory elements but lacking a transgene (hereon Control LV), to immunocompetent mice at dose ranges previously reported to target liver cells at high efficiency (Figure 2A).[15] In mice hosting IFNα LV-engineered liver macrophages, we observed rapid transgene output reflected by the detection of increasing concentrations of IFNα in plasma, peaking after 3 weeks at 700-1,000 pg/mL and stabilizing thereafter between 200 and 700 pg/mL (Figure 2B). These IFNα levels remained stable compared to the Control LV cohort for up to 240 days and eventually decreased to virtually undetectable levels by day 360. Integrated LV copies per genome in the liver of IFNα LV-treated mice were lower than those found in Control LV-treated mice, suggesting long-term counterselection of IFNα LV-transduced liver cells (Figure 2C). IFNα LV-treated mice showed decreased numbers of circulating B cells and eosinophils over time compared to Control LV-treated mice. A minor decrease was also observed for resident monocytes, red blood cells, and hemoglobin levels (Figures 2D and S2A). To investigate whether the drop in B cells may be associated to B cell activation and autoantibody production, we measured the presence of autoantibodies in the plasma of either saline (PBS), Control LV, or IFNα LV-treated mice at days 52 and 366. We found no

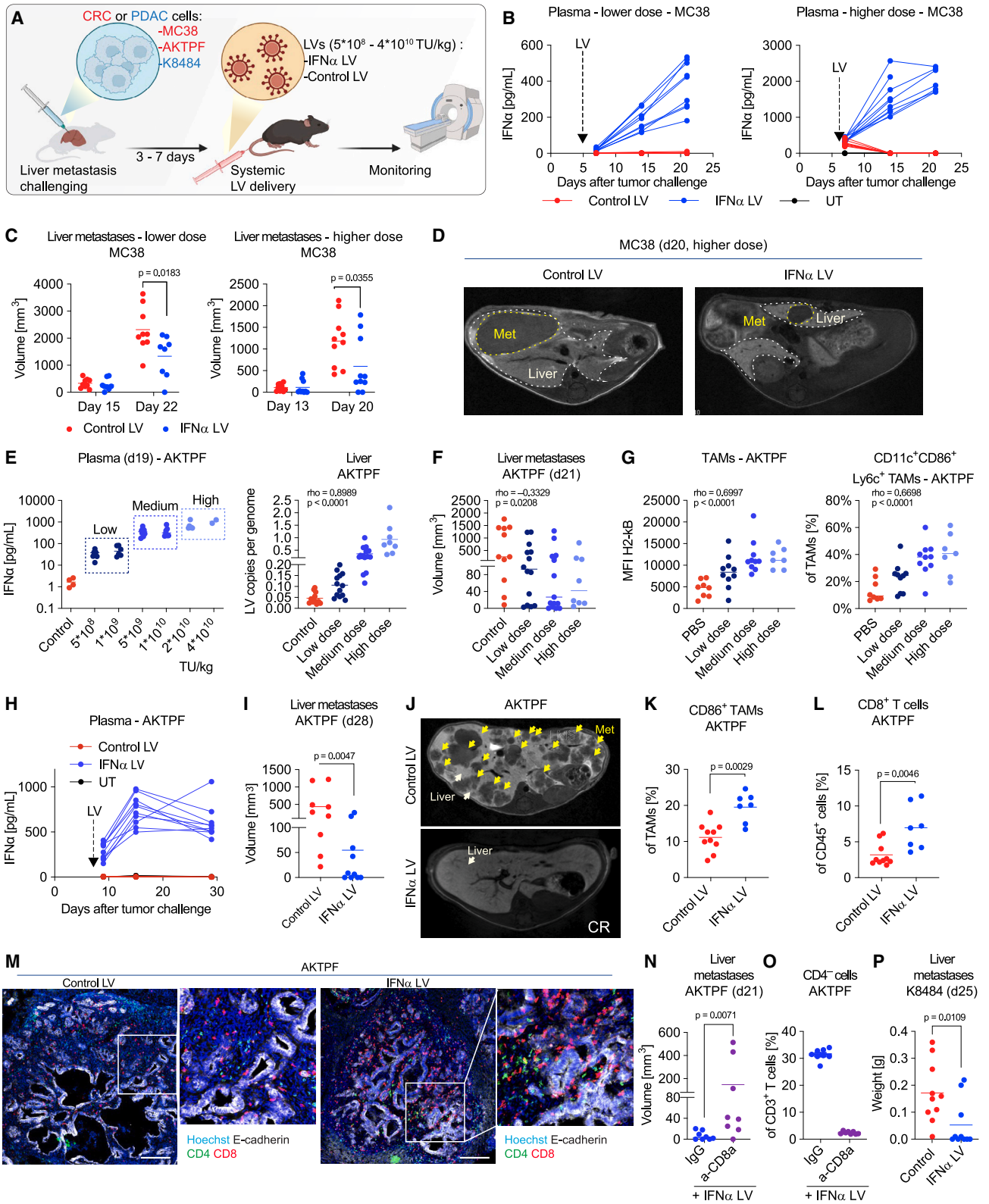

Figure 3. Gene-based enforced IFNα expression by liver macrophages unleashes T cell activation and impairs liver metastasis growth

(A) Schematics of the experiments in panels B–P.

(B–D) Therapeutic efficacy of IFNα LV at two different doses (lower dose 1.5*10^9 TU/kg and higher dose 1.5*10^{10} TU/kg) in mice bearing MC38 CRC liver metastases. LV injected at day 3 after tumor challenge. In B, plasma IFNα levels by using ELISA at the indicated time points after tumor challenge (left panel n = 10,

(legend continued on next page)

differences in the levels of autoantibodies among all the analyzed groups (Figure S2B). Furthermore, we did not observe altered levels of indicators of liver or tissue damage (i.e., alanine aminotransferase, ALT, and aspartate aminotransferase, AST) suggesting absence of hepatotoxicity in IFNα LV-treated mice (Figure 2E). To further investigate whether exogenous IFNα expression by liver macrophages induced inflammation, tissue damage, or other alterations, we performed a histopathological analysis of most relevant organs at the end of the experiment. No treatment-related abnormalities were observed in any of the analyzed compartments (Figures 2F and S2C). Taken together, these results indicate that liver macrophage-driven IFNα expression leads to robust and long-term levels of plasmatic IFNα, which were safe and well tolerated in mice.

Gene-based enforced IFNα expression by liver macrophages unleashes T cell activation and impairs liver metastasis growth

We delivered systemically 2 different doses ($1.5*10^9$ or $1.5*10^{10}$ TU/kg) of IFNα LV to engineer liver macrophages in mice previously challenged with MC38-based experimental liver metastases (Figure 3A). We found dose-dependent sustained levels of IFNα in plasma as well as dose-dependent LV copies integrated in the liver and negative association between IFNα levels in plasma and number of circulating B cells in IFNα LV-treated mice (Figures 3B, S3A and S3B). We found that both IFNα LV doses delayed tumor progression and, in 3 mice (1 for the lower and 2 for the higher dose), enabled complete response (CR) and long-term survival (Figures 3C and 3D). CR mice re-challenged with subcutaneous MC38 tumors displayed impaired tumor growth suggesting induction of adaptive immune memory against tumor-associated antigens (Figure S3C).

To further investigate the effects of enforced IFNα expression on the TME, we employed AKTPF CRC cells to generate experimental liver metastases. AKTPF liver metastases recapitulate some of the histopathological features of human CRC liver metastases, such as epithelial gland structures formed by CRC cells, dirty necrosis zones, fibrosis, angiogenesis, and immune infiltration (Figures S3D and S3E). We performed a dose-response experiment, with doses of IFNα LV ranging from $5*10^8$ TU/kg to $4*10^{10}$ TU/kg. We observed an LV dose-dependent increase in IFNα output in plasma and LV copies per genome in the liver, as well as a significant decrease in liver metastasis volume concomitant with increasing proportions of TAMs expressing markers of inflammatory phenotype (Figures 3E–3G and S3F). In line with previous data, we observed a dose-dependent decrease in the number of circulating B cells with increasing IFNα dose (Figure S3G). Histopathological analysis of the liver did not reveal hepatocellular abnormalities or increased signs of inflammation over controls at any tested doses and none of the treated mice displayed signs of liver toxicity even at the highest dose of the IFNα LV, as shown by measuring plasma transaminase levels (Figures S3H and S3I). We then performed two more independent experiments with mice bearing AKTPF liver metastases using a dose of $5*10^9$ TU/kg, selected because it provided the best therapeutic index when comparing anti-tumor effect to systemic IFNα exposure. IFNα LV delayed tumor progression and led to CR in 8 out of 20 mice in the 2 experiments (Figures 3H–3J and S3J–S3L). According to our previous findings with MC38 experimental metastasis model, we observed skewed TAMs toward an inflammatory phenotype and increased number of tumor-infiltrating $CD8^+$ T lymphocytes (Figures 3K–3M and S3M).

To investigate the induction of tumor-responsive T cells upon liver macrophage engineering, we delivered systemically the Control LV or the IFNα LV to syngeneic immunocompetent mice previously challenged with experimental liver metastases of MC38 cells expressing chicken ovalbumin (OVA, used as surrogate tumor antigen) and harvested tumors early after treatment to capture emergence of tumor-reactive T cells. In agreement with previous results, IFNα expression by liver macrophages delayed liver metastasis growth, albeit not significantly at this earlier time of analysis (Figures S3N and S3O). We found that tumor-specific T cells, identified by staining with a pentamer MHC-I complexed with an OVA immunogenic peptide (SIINFEKL), were enriched in tumors from IFNα LV-treated

10, 5; right panel, n = 10, 10, 5 mice/group). In C, tumor growth by magnetic resonance imaging (MRI) at indicated timepoints (left panel, n = 9, 8, 9, 8; right panel, n = 10, 10, 10, 10 mice/group; horizontal line represents Mean, statistical analysis by Mann-Whitney). In D, representative MRI of a Control LV- (left panel) and a IFNα LV-treated (right panel) mice bearing MC38 liver metastases, 20 days after tumor transplant, complete responder (CR), healthy liver (white) and metastasis (Met, yellow) are indicated with a dotted line.

(E–G) Therapeutic efficacy of IFNα LV at increasing doses (ranging from $5*10^8$ to $4*10^{10}$ TU/kg) in mice bearing AKTPF CRC liver metastases. LV injected at day 7 after tumor challenge. In E, plasma IFNα levels by ELISA at day 19, subdivision into treatment cohorts, and LV copies per genome in liver at endpoint (n = 7, 7, 6, 8, 7, 6, 2 mice/group from left to right, horizontal line represents Mean). In F, tumor growth by MRI at day 21 (n = 11, 14, 15, 8 mice/group from left to right; horizontal line represents Median, statistical analysis by Spearman correlation). In G, remodeling of TAMs in tumor infiltrate, respectively, in terms of antigen presentation and percentage of indicated population by FC analysis (left panel and right panel n = 8, 10, 10, 7 mice/group; horizontal line represents Median, statistical analysis by Spearman correlation).

(H–M) Therapeutic efficacy of IFNα LV at $5*10^9$ TU/kg in mice bearing AKTPF CRC liver metastases, LV injected at day 7 after tumor challenge. In H, plasma IFNα levels by ELISA at indicated time points after tumor challenge (n = 11, 10, 3 mice/group). In I, tumor growth by MRI at day 28 (n = 9, 10 mice/group; horizontal line represents Mean, statistical analysis by Mann-Whitney test). In J, representative MRI of a Control LV- (top panel) and a IFNα LV-treated (bottom panel) mice bearing AKTPF liver metastasis, 28 days after tumor transplant, complete responder (CR), healthy liver (white) and metastasis (Met, yellow) are indicated with arrows. In K and L, percentage of indicated cell populations at endpoint by FC analysis (n = 10, 7 mice/group; horizontal line represents Mean, statistical analysis by Mann-Whitney test). In M, representative IF images obtained by CM of AKTPF liver metastases, CD4 (green), CD8 (red), E-Cadherin (gray) and nuclei (blue).

(N and O) $CD8^+$ T cell depletion in IFNα LV-treated mice in a mice bearing AKTPF CRC liver metastases. LV ($5*10^9$ TU/kg) injected at day 7 after tumor challenge. In N, tumor growth by MRI analysis at day 21 (n = 8, 8 mice/group; horizontal line represents Mean, statistical analysis by Mann-Whitney test). In O, percentage of circulating $CD3^+$ $CD4^-$ T cells at day 13 by FC analysis (n = 8, 8 mice/group; horizontal line represents Mean, statistical analysis by Mann Whitney test).

(P) Therapeutic efficacy of IFNα LV at $5*10^9$ TU/kg in mice bearing K8484 PDAC liver metastases, LV injected at day 7. Tumor weight at day 25 (n = 10, 10; horizontal line represents Mean, statistical analysis by Mann-Whitney test).

See also Figure S3.

compared to Control LV-treated mice (Figure S3P). Phenotypic changes in TAMs showed a trend toward increased proportion of inflammatory phenotype, consistent with more robust findings in all other experiments in which endpoint analysis was performed at a later timepoint after LV delivery (Figure S3Q). We also observed a reversal of the IFNα antitumor efficacy in mice bearing AKTPF liver metastases upon $CD8^+$ T cell depletion (Figures 3N, 3O and S3R). To investigate whether IFNα released from engineered macrophages directly activated $CD8^+$ T cells promoting their cytotoxic activity, we employed *Cd4*^{Cre};*Ifnar1*$^{flox/flox}$ transgenic mice in which the Cre recombinase is expressed by the CD4 promoter and becomes activated in common $CD4^+$ $CD8^+$ precursor cells, leading to virtually complete knock out of the IFNAR1 receptor in both $CD4^+$ and $CD8^+$ lineages (Figure S3S). The therapeutic efficacy of IFNα LV was maintained in these mice concomitant with enhanced expression of CD44 and TBET on $CD8^+$ T cells, suggesting that IFNα indirectly activated T cells in liver metastases (Figures S3T–S3V). In agreement with previous findings, TAMs upregulated markers of antigen presentation (Figure S3W). This indicates that, although $CD8^+$ T cells are essential for IFNα LV-mediated tumor inhibition, these might not be directly activated by IFNα but rather benefit, at least in part, from the IFNα-dependent increased antigen presentation in the TME. To investigate whether additional effector mechanisms beside $CD8^+$ T cells contribute to the anti-tumor activity of IFNα LV, we tested the platform on immunodeficient NSG mice. Although liver metastases grew faster in NSG compared to immunocompetent mice, IFNα LV significantly delayed their growth compared to Control LV, albeit without achieving CR (Figures S3X and S3Y). An increased proportion of TAMs expressing markers of inflammatory phenotype upon IFNα LV was observed also in this model (Figure S3Z). Overall, these findings are in agreement with the established pleiotropic functions of IFNα, which have been shown to activate macrophages, inhibit cancer cell proliferation, and increase immune cell adhesion while impairing neo-angiogenesis by endothelial cells.[22–25] However, the lack of CR in NSG mice and the rescued tumor growth upon CD8 T cell depletion, indicate that activation of CD8 T cell-mediated immunity might be required for enabling the full therapeutic activity of IFNα LV.

To assess the protective effect of IFNα treatment on metastatic seeding and engraftment, we performed a prophylactic delivery of IFNα LV 7 days prior to AKTPF CRC injection and observed that none of the mice developed liver metastases (Figures S3AA and S3AB).

We then investigated the effect of engineered macrophage-sourced IFNα on liver metastasis arising from intrahepatic injection of *Kras*^{G12D};*Trp53*^{R172H} PDAC cells (K8484).[26] We found strong inhibition of tumor growth, including 5 CR out of 10 treated mice in the IFNα LV group compared to the Control LV group (Figures 3P, S3A and S3C). Consistent with the aforementioned findings in mice bearing CRC metastases, we found increased proportions of TAMs and $CD8^+$ T cells expressing activation markers (Figures S3AD and S3AE).

Altogether, these results indicate that liver macrophage engineering through systemic delivery of IFNα LV robustly inhibits liver metastases from different tumor types at least in part by promoting inflammatory TAM phenotypes and activation of $CD8^+$ T cell responses.

Engineering of liver macrophages by IFNα LV enables preferential IFNα signaling in peri-metastatic areas

To investigate the mechanism underlying the observed tumor response, we performed comprehensive transcriptomic analyses of AKTPF liver metastases of Control LV or IFNα LV-treated mice. We observed increased expression of interferon-stimulated genes indicating IFNα activity in the metastatic lesions of the IFNα LV cohort (Figure S4A). We then employed spatial transcriptomics to investigate, within the metastatic liver, if there were areas of preferential IFNα signaling. To this purpose, we assigned mice to three distinct cohorts: (1) Control: Control LV-treated mice, (2) Responder: IFNα LV-treated mice with reduced metastasis volume as compared to Control and, (3) Resistant: IFNα LV-treated mice with metastasis volume similar to Control (Figure S4B). Note that we could not analyze CR because of the lack of tumor at the time of analysis. Unsupervized clustering analysis was then performed to cluster spatial spots based on similar transcriptomics profile (Figures S4C and S4D). We then grouped spatial spots, according to their relative distance from the metastasis/liver parenchyma boundary, into distinct spatial compartments comprising inner metastatic (spatial compartments A–C), front metastatic (spatial compartment D), peri-metastatic (spatial compartments E−G), and intact liver areas (spatial compartment H) (Figures 4A and S4E).

As expected, we found that, in all cohorts, genes belonging to biological processes or pathways related to cancer (e.g., angiogenesis, p53 pathway, epithelial to mesenchymal transition) were enriched in the metastatic areas (inner and front areas) compared to areas outside the liver metastases (peri-metastatic and intact liver). In agreement with this observation, epithelial cell-associated genes such as *Epcam,* cadherin 1 (*Cdh1*), and villin 1 (*Vil1*) were highly expressed in inner and front metastatic areas. In contrast, hepatocyte-associated genes (e.g., albumin, *Alb*; *Apoa2,* and *Cyp27a1*) as well as gene sets belonging to liver-associated pathways (e.g., adipogenesis or bile acid metabolism) were upregulated in intact liver areas (Figure 4B). In agreement with enhanced transgene expression from engineered KCs in areas surrounding liver metastases upon systemic *Mrc1*.GFP.miRT LV delivery, we found that genes associated with response to type I interferon (e.g., *Socs1*, *Stat1*, and *Nlrc5*) were enriched in liver metastasis and peri-metastatic areas of the IFNα LV cohort (responder and resistant), confirming the capacity of the LV platform to preferentially engineer KCs in proximity to liver metastases. Moreover, upregulation of genes related to type I interferon activity and belonging to gene ontology (GO) categories such as response to interferon gamma, response to virus, positive regulation of cytokine production, and T cell activation were associated with areas of type I interferon signaling. Furthermore, in responder compared to resistant or control cohorts, genes belonging to adaptive immune activation GO categories, such as adaptive immune response (e.g., *Cd3g*, *Cd8a*, and *Trac*) and regulation of immune effector process were upregulated in inner, front, and peri-metastatic areas, corresponding to sites of enhanced IFNα activity. Genes associated with antigen presentation (e.g., *Cd86*, *H2-Oa*, and *Tap1*) were also highly expressed in metastatic lesions of both responder and resistant cohorts compared to control. Importantly, in the resistant cohort, but not in the control or responder, we found increased IL-10 signaling in front and peri-metastatic areas,

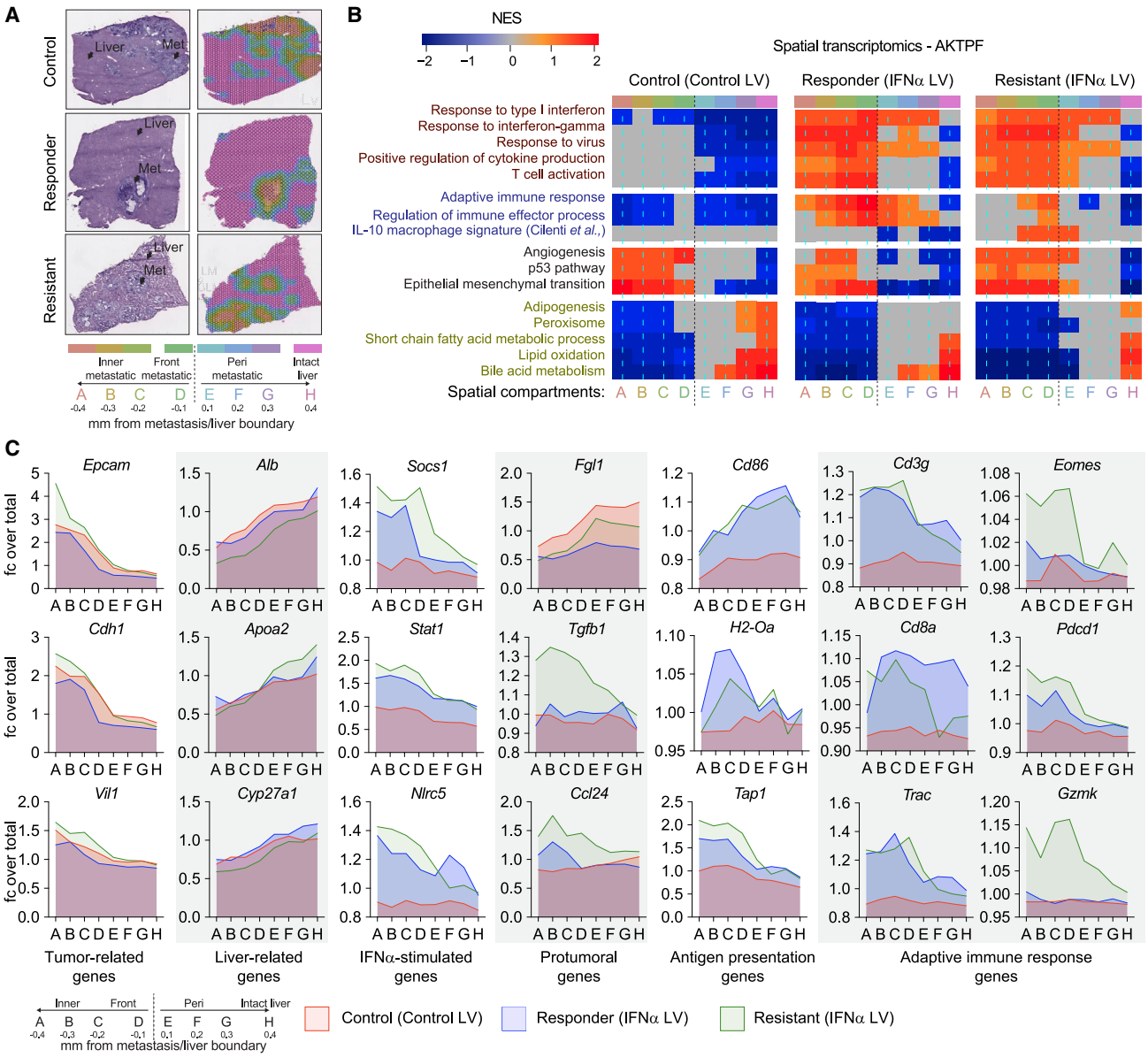

Figure 4. Engineering of liver macrophages by IFNα LV enables preferential IFNα signaling in peri-metastatic areas

(A) Side-by-side comparison of representative liver sections containing metastatic lesions (Met) from the indicated treatment cohorts analyzed by spatial transcriptomics showing the H&E-stained (left) or analyzed by using spatial transcriptomics (right). Spatial spots are indicated in a color associated to a spatial compartment.

(B) Heatmap displaying gene set enrichment analysis (GSEA) normalized enrichment score (NES) for selected gene ontology (GO) terms across distinct spatial compartments by spatial transcriptomics (Visium). Gene sets are grouped into cytokine related effects (red), immune activation state (blue), tumor associated (black), and hepatic functions (olive; n = 3, 3, 2 mice/group).

(C) Fold change (fc) over average gene expression level for the indicated genes belonging to the indicated gene categories in the spatial compartments and treatment cohorts (n values as in B).

See also Figure S4 and Table S1.

suggesting that IL-10 might counteract, at least in part, IFNα-mediated immune effect in resistant mice. Of note, markers associated with exhaustion and tolerogenic phenotype of T cells such as *Tgfb1*, *Eomes*, and *Gzmk* were also upregulated in the resistant group in inner, front, and peri-metastatic areas (Figures 4B and 4C; Table S1). Altogether, IFNα expression by liver macrophages was associated with selective immune activation in liver metastases and peri-metastatic areas of responder mice. However, in resistant mice, immune activation appeared dampened compared to responders and was associated with an enrichment of IL-10 signaling in the metastasis/liver parenchyma boundary area.

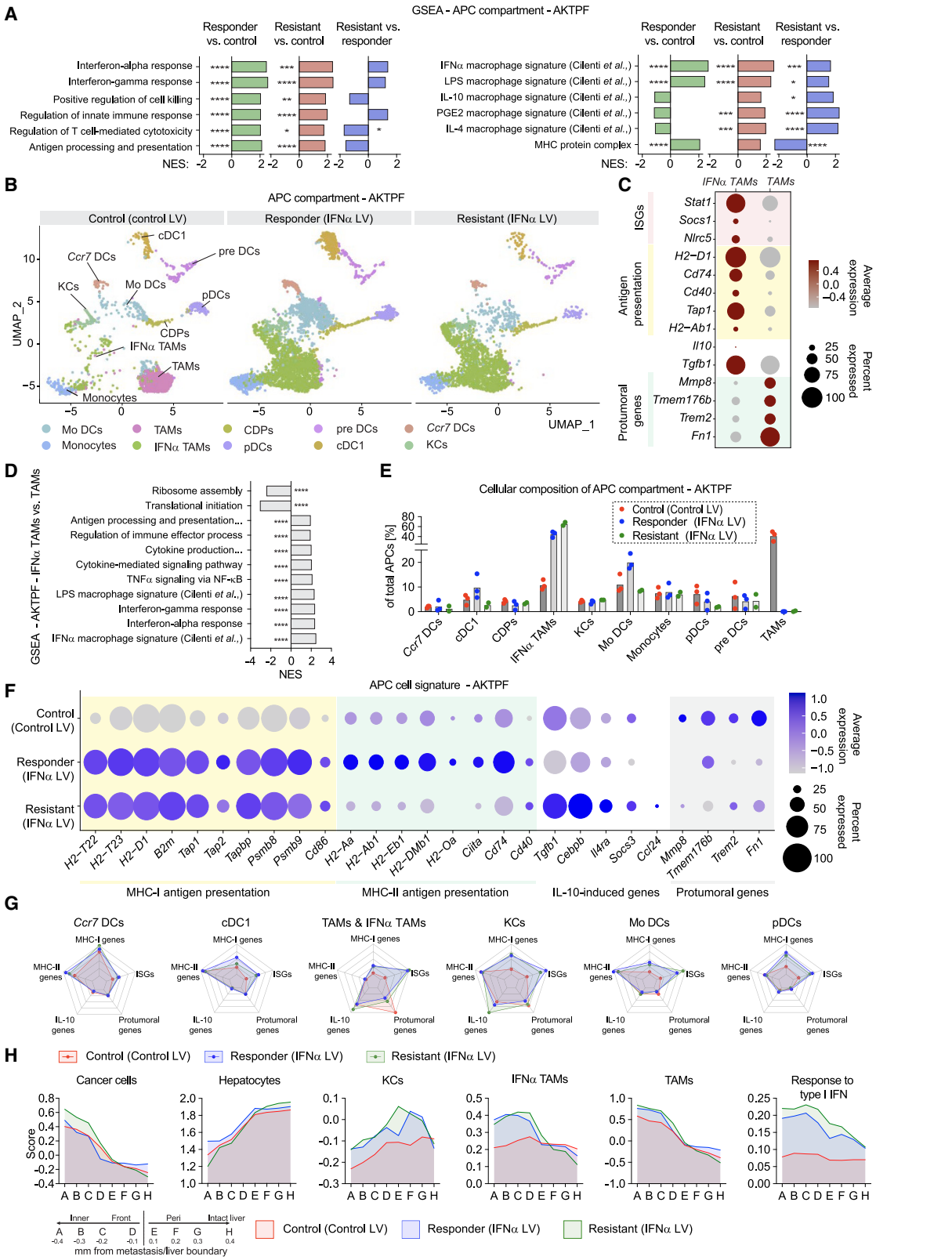

(legend on next page)

IFNα promotes APC immune activation and enhanced MHC-II-restricted antigen presentation in responder mice

We performed single-cell transcriptomics on live cells from the same metastatic lesions assayed by spatial transcriptomics (Figure S4B). We employed an unsupervized clustering method to identify distinct cell types, such as (1) APCs, (2) T and NK cells, (3) B cells, (4) neutrophils, (5) endothelial cells, (6) hepatocytes, (7) cancer cells, which were manually annotated based on their transcriptomic profile (Figures S5A–S5D; Table S2). We then focused on cells belonging to the APC cluster. We found that genes belonging to GO categories related to IFNα, IFNγ, or LPS signaling were relatively enriched in all IFNα LV-treated cohorts. On the other hand, genes linked to IL-10, PGE2, and IL-4 signaling were upregulated in the resistant compared to the responder cohort, suggesting that these genes might play a role in inducing resistance to gene-based IFNα therapeutic activity. Genes linked to antigen presentation, i.e., MHC protein complex and antigen processing and presentation, were upregulated in the partial responder compared to resistant or control cohorts and showed the lowest expression in the control cohort (Figure 5A). We then performed a sub-clustering analysis to better define cell populations and differentially expressed genes within the APC cluster. Within APCs, we found overlapping cell clusters in all three experimental cohorts, with the exception of the TAM cluster, which was reshaped by IFNα treatment, indicating gene expression reprogramming upon exposure to gene-based IFNα delivery. Building on this observation and considering the predominant effect of IFNα on TAM genetic program, we termed all TAMs belonging to the cluster present in IFNα LV-treated tumors IFNα-TAMs, while those present in the control LV cohort were termed TAMs. All the other cellular clusters were manually annotated based on their gene expression profile (Figures 5B and S5E). By employing differential gene expression analysis between TAM subsets, we found that genes upregulated in IFNα-TAMs compared to TAMs, for all three cohorts, were enriched in biological processes related to IFNα/IFNγ response, such as *Stat1*, *Socs1*, and *Nlrc5*; TNFα signaling; LPS activation; and antigen processing and presentation, such as MHC subunits (*H2-D1* and *H2-Ab1, Cd74*), *Cd40* and *Tap1* in line with a role of IFNα-TAMs in positively regulating immune activation. On the other hand, protumoral genes commonly associated with TAM protumoral activities, such as *Mmp8*, *Tmem176B*, *Trem2*, and *Fn1* were upregulated in TAMs vs. IFNα-TAMs (Figures 5C and 5D). Of note, professional APCs, i.e., classical dendritic cells (cDCs) and monocyte-derived DCs (Mo DCs) were enriched in the responder cohort compared to resistant and control cohorts (Figure 5E). In agreement with this observation, we found that, in APCs from responder mice, genes associated with MHC-II-restricted antigen presentation such as genes encoding for MHC-II subunits (*H2-Aa*, *H2-Ab1*, *H2-Eb1*, *H2-DMb1*, and *H2-Oa*), MHC-II transactivator (*Ciita*), *Cd74* and *Cd40* were upregulated compared to resistant or control mice. Of note, MHC-I-restricted genes, such as genes encoding for MHC-I subunits (*H2-T22*, *H2-T23*, *H2-D1,* and *B2m*), *Tap1*, *Tap2*, tap binding protein (*Tapbp*), and proteasome S20 subunit beta 8 and 9 (*Psmb8* and *Psmb9*) were upregulated in all IFNα LV-treated (resistant and responder) cohorts. In agreement with IL-10 playing a putative role in resistance to liver macrophage-derived IFNα expression, IL-10-associated genes, such as *Tgfb*, *Cebpb*, *Il4r*, *Socs3*, and *Ccl24* were upregulated in APCs of the resistant compared to the responder and control cohorts (Figure 5F). Out of all the APC populations, *Ccr7*-expressing DCs, cDCs and KCs and Mo DCs expressed the highest levels of genes related to MHC-II-restricted antigen presentation in all cohorts. Therefore, differences in expression level of genes related to MHC-II-restricted antigen presentation in APCs may be, at least in part, attributed to enhanced infiltration of professional APCs, such as Mo DCs and cDCs in the responder cohort. On the other hand, upregulation of genes related to MHC-I-restricted antigen presentation may be caused by a direct effect of IFNα (Figure 5G). In summary, IFNα released from liver macrophages promoted APC reshaping toward an immunostimulatory phenotype through boosting antigen presenting functions. However, MHC-II-restricted functions and DC infiltration appeared reduced in resistant compared to responder mice. Concomitantly, IL-10 signaling was enhanced in APCs from resistant mice, hinting toward an association between lack of response to IFNα, IL-10 upregulation, and impaired MHC-II-restricted antigen presentation.

Although LV dependent IFNα signaling was predominant in defining the skewing of TAMs, by masking this effect employing harmonization methods, we were able to collapse TAMs from the two treatments into overlapping but heterogeneous subclusters and uncovered an IFNα LV-dependent lower contribution to subclusters marked by genes associated to pro-tumoral activity, while increasing the contribution to subclusters marked by pro-inflammatory markers (Figures S5F–S5H). Genes associated to IFNα signaling and MHC-I presentation were generally upregulated in all TAM subclusters by IFNα LV treatment (Figure S5I).

By using gene signatures derived from our single cell analysis or from established KC markers, we deconvoluted the spatial transcriptomics data from Figure 4 and found that TAM signatures had the highest score in the inner tumor (area A to D) and

Figure 5. IFNα promotes APC immune activation and enhanced MHC-II-restricted antigen presentation in responder mice

(A) GSEA of single-cell RNA (scRNA) sequencing data showing NES for selected GO terms calculated based on genes differentially expressed in antigen-presenting cells (APCs) in the indicated comparisons (n = 3, 3, 2 mice/group for control, responder and resistant; statistical analysis by an adaptive multi-level split Monte-Carlo scheme; *: padj <0.05; **: padj <0.01; ***: padj <0.001; ****: padj <0.0001).

(B) UMAP projection of scRNA sequencing data of APCs for the indicated groups.

(C) Expression of selected genes belonging to the indicated categories in IFNα TAMs and TAMs.

(D) GSEA showing NES of selected GO terms on genes differentially expressed in IFNα TAMs vs. TAMs (n = 8 mice/group; statistical analysis as in A).

(E) Percentage of cells within the indicated populations belonging to the APC compartment (n as in a).

(F) Gene expression of genes belonging to indicated categories in the APC compartment.

(G) Combined gene expression score of genes belonging to the indicated categories in the different cell populations from the indicated cohorts.

(H) Distribution of indicated populations after deconvolution of spatial transcriptomics data.

See also Figure S5 and Tables S2 and S3.

sharply decreased moving toward the healthy parenchyma (area E to H), while a KC signature had a low score inside the tumor and increased in the peri-metastatic area (area E to G) and intact tissue (H), in agreement with biodistribution analysis of Figure 1 (Figure 5H; Table S3). Interestingly, in IFNα LV-treated mice, the KC signature score was higher in all tumor areas and peaked in the peri-metastatic one, suggesting enhanced recruitment, activation or proliferation of these cells.

Therapeutic response to IFNα is associated with T cell activation and is counteracted by *Eomes* CD4$^+$ T cell infiltration

We then performed differential expression analysis in the T and NK cell compartment among the three experimental cohorts. Similar to TAMs, genes belonging to IFNα and IFNγ signaling were enriched in all IFNα LV-treated cohorts. Conversely, genes belonging to immune activation (i.e., T cell-mediated cytotoxicity, natural killer cell activation, or regulation of cell killing) were upregulated exclusively in the partial responder cohort (Figure 6A). We then performed an unsupervized sub-clustering analysis to identify distinct cell populations within the T and NK cell compartment and manually annotated the resulting clusters. We found overlapping cell clusters in all three experimental cohorts (Figures 6B and S6A; Table S4). Selectively in resistant mice, we observed a population of regulatory CD4$^+$ T cells, which transcriptionally resembled previously described Tr1 cells (hereon termed *Eomes* CD4$^+$ T cells)[7,27] expressing markers of CD4$^+$ T cell exhaustion, such as *Ctla4*, *Gzmk*, *Lag3*, and PD-1 (*Pdcd1*), as well as genes associated with immune suppression such as IL-10 receptor (*Il10ra*), *Il10* and the transcription factor *Eomes,* and lacking expression of the transcription factor *Foxp3* (Figures 6C and S6B). On the other hand, selectively enriched in the responder cohort, we observed a population of CD8$^+$ T effector 1 cells (Figure 6D). The latter displayed a transcriptomic signature resembling tissue-resident effector memory T cells, which were previously associated with response to immunotherapy (Figures 6E and S6B).[28] Moreover, IFNα released by liver macrophages increased IFNα and IFNγ signaling on CD8$^+$ T cells compared to the control cohort (Figure S6C). Of note, genes associated to T cell exhaustion, such as *Pdcd1*, *Lag3*, TIM-3 (*Havcr2*), *Ctla4*, *Eomes*, *Tox*, *Ccl3*, *Ccl4*, and *Casp3*, were downregulated in responder compared to control or resistant mice (Figure 6E). In contrast, genes associated with adaptive immune response and T cell-mediated immunity and cytotoxicity, such as *Tcf7*, *Tbx21*, *Cd69*, *Itgae*, *Itga1*, *Cd7*, *Il2*, and *Tnf* were more upregulated in responder than in resistant mice. Altogether, these data indicate that IFNα released by engineered macrophages promoted adaptive immunity in responder mice by reshaping the T cell infiltrate enriching for effector phenotypes associated with response to immunotherapy while dampening T cell exhaustion. Conversely, in resistant mice, infiltrating *Eomes* CD4$^+$ T cells and enhanced exhaustion of CD8$^+$ T cells may prevent anti-tumor effect.

Higher IFNα signaling correlates with increased Tr1 gene signature in human liver CRC metastases

We then investigated whether also in human CRC liver metastases IFNα signaling was positively associated with the presence of *Eomes* CD4$^+$ T cells in the TME. To this aim, we employed bulk RNA sequencing data from human CRC liver metastases collected from our center and found that patients with higher IFNα signaling score displayed higher levels of Tr1 signature score (Figures 7A, 7B and S7A). We then analyzed peri-metastatic and metastatic liver areas from patients bearing CRC liver metastases by employing nanostring RNA technology. In agreement with bulk RNA results and our mouse data, we observed a positive correlation between IFNα score and Tr1 score, *CTLA4* expression and *HLA-C* expression in both peri-metastatic and metastatic areas (Figure 7C). Moreover, genes involved in antigen presentation, immune cell activation, or other IFNα-stimulated genes not included in the signature employed to calculate the IFNα score were positively correlated with IFNα score (Figure 7D).

We then performed immunostaining on CRC liver metastasis samples from eleven patients in this cohort, respectively, 6 patients with high and 5 patients with low-IFNα signaling score. We observed higher percentages of LAG3$^+$ CD4$^+$ T cells infiltrating patient metastases within the IFNα high group compared to IFNα low group (Figures 7E and S7B). Of note, LAG3 was previously reported as a marker of T cell exhaustion and also of human Tr1 cells.[29] We then performed a case study analysis of two patients within the IFNα high-signaling group and observed the presence of triple positive LAG3$^+$ EOMES$^+$ CD4$^+$ T cells and CTLA-4$^+$ CD4$^+$ T cells infiltrating the tumor (Figure 7F). In agreement with this finding, the percentage of CD4$^+$ T cells expressing CTLA-4 was higher in the IFNα high compared to the IFNα low group (Figure S7C). Overall, these findings suggest that Tr1-like cells, as well as CTLA-4 expression, positively associate with endogenous IFNα signaling and may, at least in part, counteract immune activation in the TME.

IFNα from engineered liver macrophages in combination with functional inhibition of regulatory T cells eradicates liver metastases

In mice resistant to IFNα LV, we found increased IL-10 signaling, lower expression of MHC-II antigen presentation genes, enhanced *Eomes* CD4$^+$ T cell infiltration and enhanced CD8$^+$ T cell exhaustion. This observation is in agreement with previous studies that indicate that IL-10 may play a role in the differentiation, accumulation, and effector function of *Eomes* CD4$^+$ T cells,[30,31] which have been described to suppress antigen presentation through perforin-mediated direct killing of DCs[32] and suppress T cell activities in CRC liver metastases through IL-10 secretion.[33] Building on these observations, we inhibited IL-10 signaling by using a monoclonal antibody blocking IL-10 receptor (a-IL-10R). Mice challenged with AKTPF liver metastases and treated with IFNα or Control LVs were then subjected to serial administration of either a-IL-10R or an unrelated IgG. Anti-IL-10R blocked IFNα-induced accumulation of *Eomes* CD4$^+$ T cells, indicating that IL-10 signaling is necessary for this response in liver metastases. However, the combination of IFNα and a-IL-10R achieved lower therapeutic effect than IFNα LV, suggesting that IL-10 signaling may be necessary for the deployment of IFNα therapeutic activity (Figures 8A, 8B and S8A). Of note, the combination of a-IL-10R and IFNα LV increased PD-1 expression on circulating T cells, supporting a role of IL-10 in tuning the phenotype of T cells in presence of IFNα (Figure S8B).

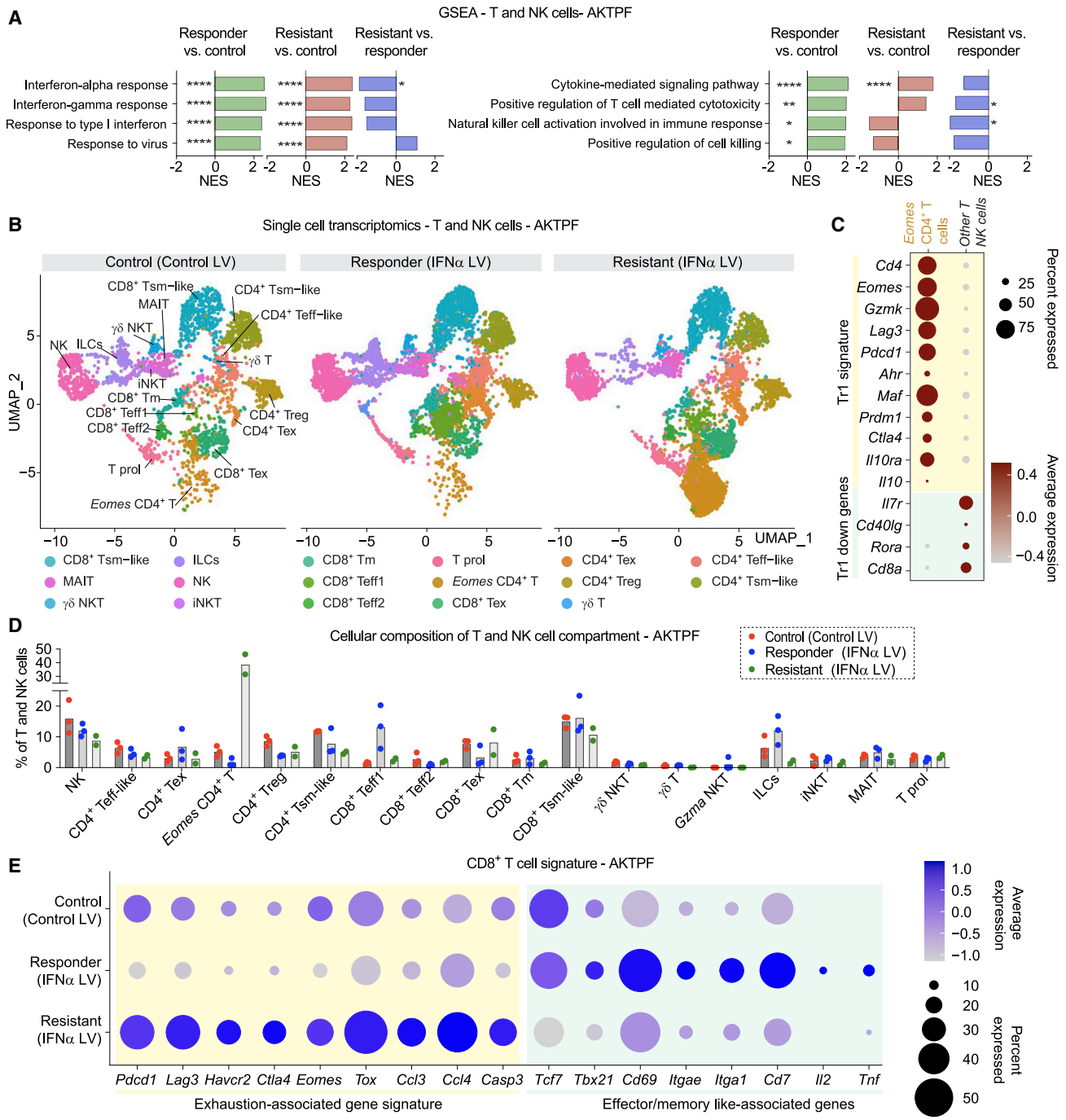

Figure 6. Therapeutic response to IFNα is associated with T cell activation and is counteracted by *Eomes* CD4⁺ T cell infiltration

(A) GSEA showing NES for selected GO terms on genes differentially expressed in the indicated comparisons (n = 3, 3, 2 mice/group in control, responder or resistant; statistical analysis by an adaptive multi-level split Monte-Carlo scheme; *: padj <0.05; **: padj <0.01; ***: padj <0.001; ****: padj <0.0001).

(B) UMAP representation of cells from AKTPF liver metastasis annotated as T and NK cells.

(C) Gene expression of Tr1 signature genes in *Eomes* CD4⁺ T cells and all other T and NK cells pooled.

(D) Percentage of the indicated cell populations for the indicated groups (n as in A).

(E) Gene expression in all CD8⁺ T cell subtypes highlighting exhaustion-associated genes and effector/memory like-associated genes highlighted in yellow or green, respectively.

See also Figure S6 and Table S4.

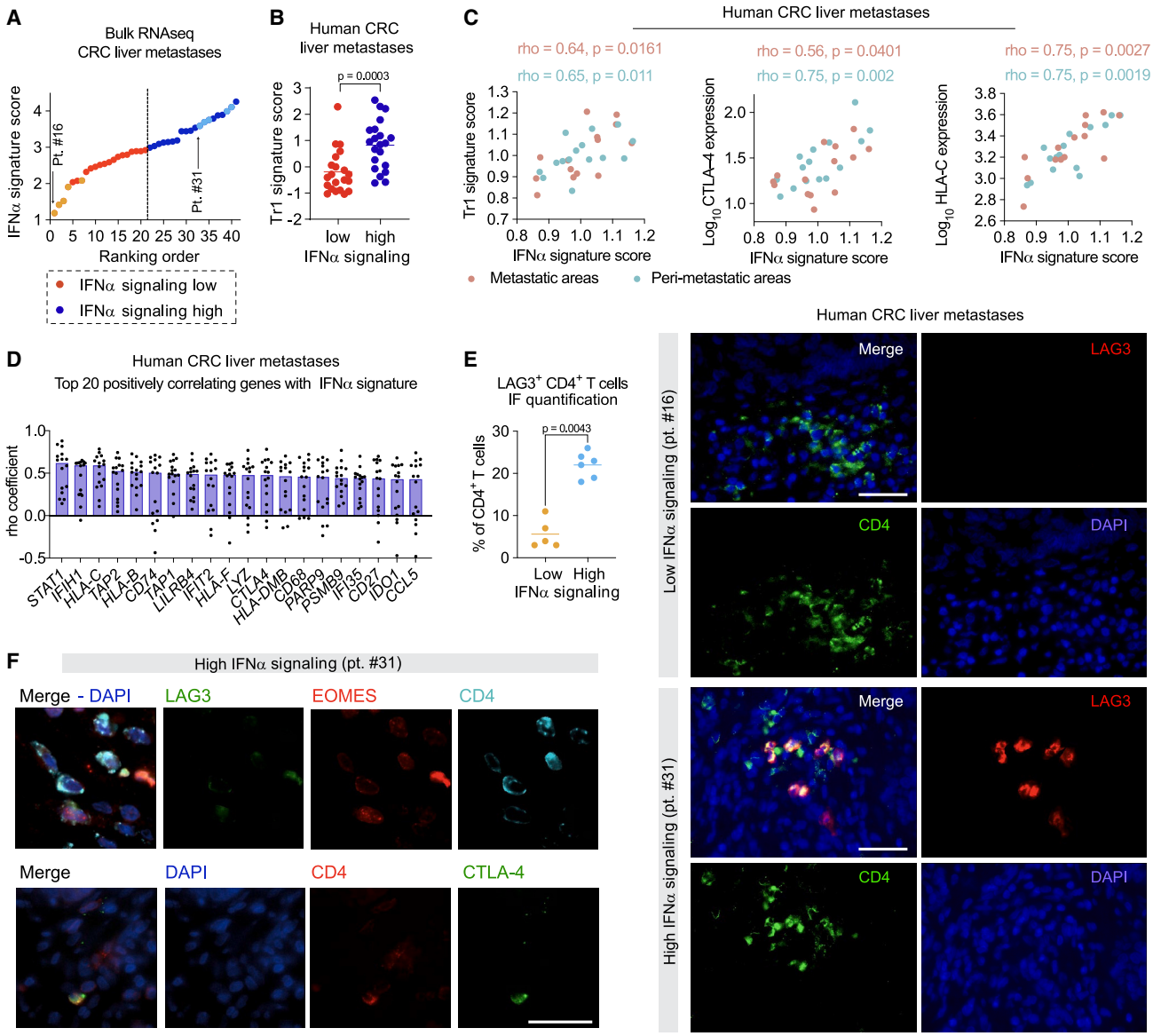

Figure 7. Higher IFNα signaling correlates with increased Tr1 signature in human CRC liver metastases

(A) Stratification of patients in IFNα-signaling low and high cohort based on their IFNα signature score by bulk RNA sequencing of CRC liver metastases (n = 42 patients).

(B) Tr1 cell signature score detected in bulk RNA sequencing data from human patient CRC-derived liver metastasis stratified by their intrinsic IFNα signaling score (n = 21 patients/group, horizontal line represents Mean, statistical analysis by Mann-Whitney test).

(C and D) Nanostring analysis on metastatic and peri-metastatic liver areas from 15 patients with CRC liver metastases. In C, correlations between IFNα signature score and TR1 signature score, CTLA-4 expression and HLA-C expression (n = 14, 15 patients/group for metastatic and peri-metastatic areas respectively; statistical analysis by Spearman correlation). In D, top 20 positively correlating genes with IFNα signature. Each point represents the correlation coefficient between a gene in the IFNα signature and the indicated gene in the x axis (n = 29 samples including both metastatic and peri-metastatic areas, line represents Median, statistical analysis by Spearman correlation).

(E) Representative IF images of CRC liver metastases from 2 patients (pt.#31, IFNα high signaling; pt.#16, IFNα low signaling) and relative quantification of LAG3$^+$ cells out of CD4$^+$ cells showing CD4 (green), LAG3 (red), and nuclei (blue; n = 5 for IFNα low and n = 6 for IFNα high signaling; horizontal line represents Mean, statistical analysis by Mann-Whitney test; scale bar 50 μm).

(F) Representative images from one patient (pt.#31) within the IFNα high signaling group, top panel staining for nuclei (blue), LAG3 (green), EOMES (red), and CD4 (acqua). In bottom panel nuclei (blue), CD4 (red), and CTLA-4 (green). Scale bar 50 μm.

See also Figure S7.

We observed that *Ctla4* was expressed in *Eomes* CD4$^+$ T cells, exhausted CD4$^+$ and CD8$^+$ T cells and *Foxp3* T regulatory (Treg) cells (Figure S6B). Furthermore, *Ctla4* was strongly upregulated in CD8$^+$ T cells in the resistant mice. Of note, CTLA-4 in Tr1 cells may play a key role in suppressing T cell functions[34] as well as in attenuating antigen presentation by sequestering the

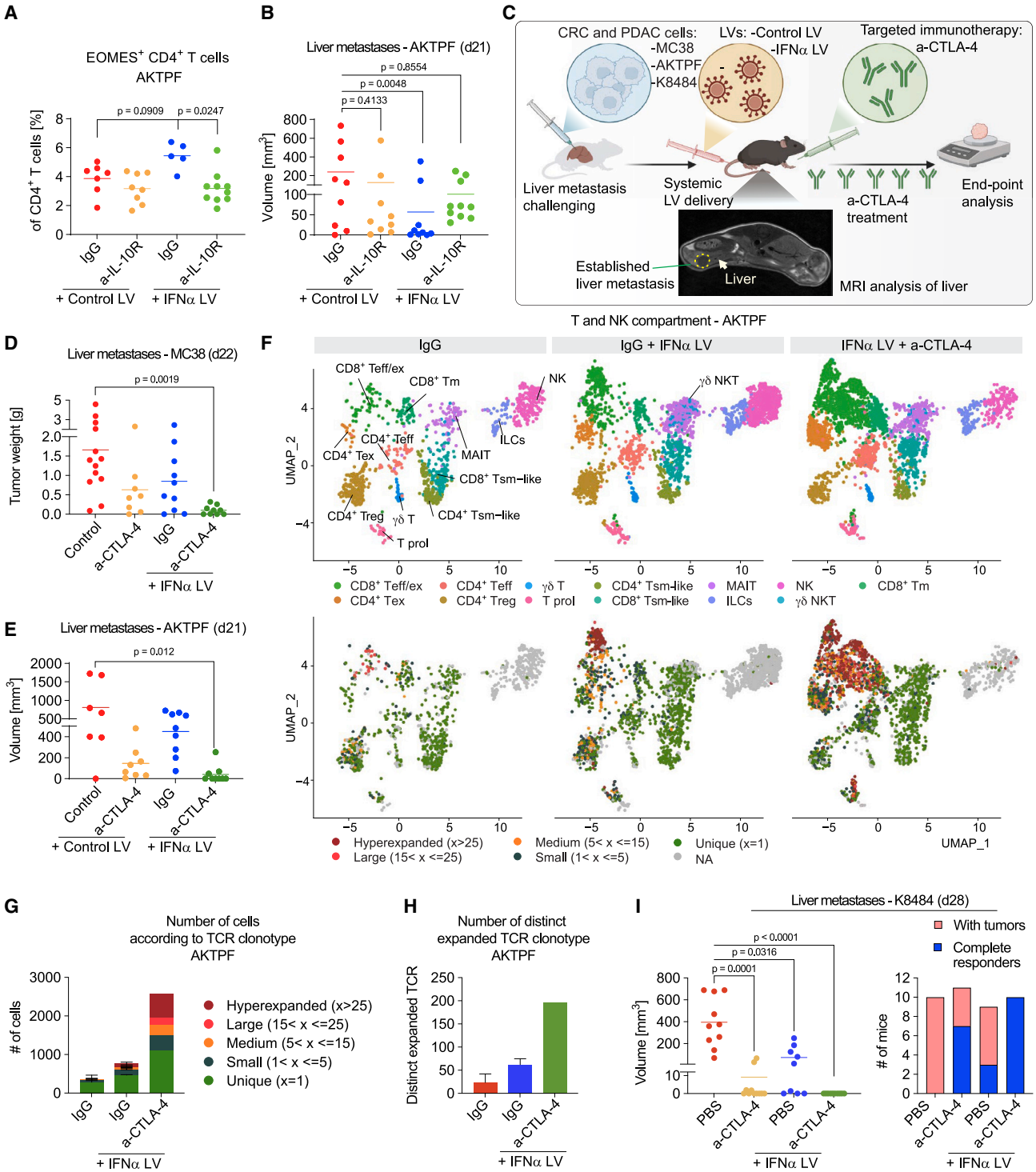

Figure 8. IFNα from engineered liver macrophages in combination with functional inhibition of regulatory T cells eradicates liver metastases

(A and B) IFNα LV combination with anti-IL-10R antibody. LV injection (dose $5*10^9$ TU/kg) at day 7 after tumor challenge. In A, percentage of EOMES $CD4^+$ T cells infiltrating AKTPF liver metastases by FC analysis (n = 7, 8, 5, 10 mice/group; horizontal line represents Mean, statistical analysis by Mann-Whitney test, p values adjusted by Bonferroni's correction). In B, tumor growth by MRI at day 21 (n = 9, 9, 9, 10, horizontal line represents Mean, statistical analysis by ANCOVA).

(C) Schematics of the experiments shown in D-I containing representative MRI analysis of a mouse 7 days after intrahepatic delivery of MC38 cells. To note the macroscopic metastatic mass present at the beginning of treatment.

(D) Therapeutic efficacy of IFNα LV in combination with a-CTLA-4 antibody in mice bearing MC38 CRC liver metastases. LV injection (dose $5*10^9$ TU/kg) at day 7 after tumor challenge. Tumor growth assessed by tumor weight at day 22. (n = 13, 8, 10, 9 mice/group, Control consists of 10 Control LV mice and 3 UT mice; horizontal line represents Mean, statistical analysis by Mann-Whitney test, p values adjusted by Bonferroni's correction).

(legend continued on next page)

costimulatory molecules CD80/CD86 in APCs.[35] Building on this observation, we combined liver macrophage-based IFNα delivery with an anti-CTLA-4 blocking monoclonal antibody administration regimen (a-CTLA-4, Figure 8C). The combination of IFNα by liver macrophages with a-CTLA-4 strongly inhibited liver metastasis growth as compared to either treatment alone in two distinct experimental models of CRC liver metastases, the MC38 and AKTPF (Figures 8D, 8E, S8C and S8D). Remarkably, in mice hosting AKTPF liver metastases, we observed up to 70% of the mice displaying complete response upon IFNα and CTLA-4 combination. This result indicates that potentiating antigen presentation in APCs through inhibition of CTLA-4 in regulatory *Eomes* $CD4^+$ T cells, exhausted CD4/$CD8^+$ T cells, and $CD4^+$ Treg cells strongly enhanced the therapeutic activity of IFNα LV, uncovering a major contribution of CTLA-4 to the development of therapy resistance.

We then repeated the experiment and harvested metastases at an early time post-treatment to perform single-cell transcriptomics and TCR clonality analysis on live cells (Table S5). While we reproduced our earlier finding of APC reprogramming by IFNα LV, the combination with a-CTLA-4 further enhanced the upregulation of genes associated with MHC-I and -II antigen presentation, and further reduced genes associated with IL-10 signaling and pro-tumoral function (Figures S8E and S8F). Within the T cell compartment, we observed an expansion of activated $CD8^+$ T cells that was strongly enhanced by the combination with a-CTLA-4 treatment. These $CD8^+$ T cells displayed features of tumor-reactive exhausted cells, as indicated by the association of this cluster with hyperexpanded TCR clonotypes and the expression of several activation/exhaustion markers such as PD-1 (*Pdcd1*), TIM-3 (*Havcr2*), *Ifng*, CD39 (*Entpd1*), *Itga1*, *Cxcr6*, and *Prf1* (Figures 8F, 8G and S8G). The combination treatment also increased the TCR clonal diversity of these expanded T cells, likely through promotion of antigen presentation by the reshaped myeloid compartment (Figure 8H). Interestingly, we observed increased expression of genes previously described as associated with tumor reactivity and effector functions in expanded T cell clones (Figure S8H).[36] Of note, we did not observe *Eomes* $CD4^+$ T cells in our second single-cell transcriptomic analysis in agreement with the selection of mice responding to the treatment. Overall, these findings demonstrate a powerful synergy between IFNα release from engineered liver macrophages and checkpoint blockade targeting regulatory T cell functions.

To confirm the effects observed with the combinatorial IFNα LV and a-CTLA-4 therapy on CRC metastases, we challenged it in mice bearing PDAC liver metastases (K8484 cells). Whereas both IFNα LV and a-CTLA-4 treatments alone were efficacious in inhibiting metastases growth, only their combination achieved full CR in all treated mice (Figures 8I and S8I).

Overall, these findings demonstrate a powerful synergy between our strategy of gene-based IFNα delivery through engineered liver macrophages from within the tumor bed and CTLA-4 blockade targeting regulatory T cell functions.

DISCUSSION

We developed an LV platform to engineer KCs in proximity to liver metastases as well as TAMs. Gene-based IFNα release in CRC and PDAC liver metastasis mouse models led to substantial TME reprograming and complete tumor eradication in some mice. Mice resistant to treatment showed increased IL-10 signaling, reduced MHC-II-restricted antigen presentation in APCs, enhanced expression of CTLA-4 in T cells and emergence of an *Eomes*-expressing $CD4^+$ T cell population transcriptionally resembling Tr1 cells, which are associated with immunosuppressive and tolerogenic functions.[27] Co-administration of CTLA-4 blockade with IFNα LV overcame these resistance mechanisms and strongly expanded tumor-reactive T cell clonotypes enabling nearly complete therapeutic responses.

Transgene output was enriched in peri-metastatic areas, possibly due to tumor-driven changes in the local vasculature undergoing remodeling, macrophage phagocytic activity and previously described increased MRC1 expression by macrophages in the presence of tumors.[19] Although TAMs populate the intra-metastatic area to a higher extent than KCs, in the overall liver, GFP^+ TAMs were a smaller fraction compared to GFP^+ KCs. Thus, liver resident KCs mostly contributed to the transgene output. It is possible that KCs are better transduced than intra-tumoral macrophages because of their natural localization in the hepatic microvascular linings. Whether these KCs become embedded in the tumor by vascular co-option or active recruitment followed by local proliferation, and whether they are as long-lived within the tumor as in intact liver, remain unknown. Of note, the preferential vector expression in KCs may explain the prolonged duration of IFNα release in our setting and support a sustained therapeutic effect.

It has been proposed that macrophages, including KCs, in the presence of tumors rewire their genetic programs to promote tumor growth and immune evasion.[37] Therefore, expression of IFNα directly in these cells may reshape their protumoral genetic programs, leading to higher therapeutic benefit. Moreover, expression from within the tissue, through liver macrophage engineering, bypasses the biodistribution, and vascular barriers of systemic administration, likely achieving more effective concentration on the target cells within the TME. Whereas systemic IFNα

(E) Therapeutic efficacy of IFNα LV in combination with a-CTLA-4 antibody in mice bearing AKTPF CRC liver metastases. LV injection (dose $5*10^9$ TU/kg) at day 7 after tumor challenge. Tumor growth by MRI analysis at day 21. (n = 7, 8, 9, 9 mice/group; horizontal line represents Mean, statistical analysis as in D).
(F–H) Single cell transcriptomics analysis of mice treated with IFNα LV, with or without combination with a-CTLA-4 antibody in mice bearing AKTPF CRC liver metastases. LV injection (dose $5*10^9$ TU/kg) at day 9, processing of tissues for scRNA sequencing at day 18. In F, UMAP representation of scRNA sequencing data of T and NK compartment for the indicated groups with associated distribution of TCR clonality. In G, number of cells according to TCR clonotype frequency (n = 2, 2, 1 mice/group; Mean +SD). In H, number of distinct expanded TCR clonotypes (n = 2, 2, 1 mice/group; Mean +SD).
(I) Therapeutic efficacy of IFNα LV in combination with a-CTLA-4 antibody in mice bearing K8484 PDAC liver metastases. LV injection (dose $5*10^9$ TU/kg) at day 7. Tumor growth by MRI analysis at day 28 and differentiation between complete responders and mice with tumors at endpoint (n = 10, 11, 9, 10; horizontal line represents Mean, statistical analysis by Kruskal-Wallis test, p values adjusted by Bonferroni's correction).
See also Figure S8 and Table S5.

administration has been associated with significant toxicity in preclinical models and in humans, we did not collect evidence of tissue damage or autoimmunity in our study even upon dose escalation. This may be due to: (i) improved therapeutic index of IFNα locally produced in the liver stroma and preferential IFNα signaling in the liver areas harboring liver metastases, (ii) stable expression of IFNα compared to peak and trough dynamics in plasma from systemically delivered cytokines, which is often associated to desensitization and toxicity,[38] (iii) plasma levels of IFNα within the physiological range and similar to those observed upon viral infections.[39,40]

Of note, LV-based cell engineering results in integration of the vector and sustained transgene expression, which may be long enough for effective therapeutic benefit. Importantly, our strategy eventually reached virtual extinction upon 1 year. Termination of expression was likely due to turnover of the engineered liver macrophages, which appeared faster for cells expressing exogenous IFNα than for those transduced with Control LV, suggesting counter selection of the former ones. Alternatively, it might be possible to employ integrase defective (ID) LVs, which persist in the nucleus as episomal forms driving lower and more transient transgene expression.[41] Whether employing LVs or IDLVs may thus depend on the desired transgene output in terms of level and duration.

Despite the therapeutic activity observed upon liver macrophage engineering through IFNα LV as a single dose treatment, a population of *Eomes* $CD4^+$ T cells, displaying a Tr1-like gene signature, counteracted IFNα action in a fraction of resistant mice. In agreement with previous reports, we showed that *Eomes* $CD4^+$ T cell development depends on type I IFN and IL-10 stimulation.[42] This observation highlights the complex and sometimes opposite effects of IFNα, which in some circumstances can promote tumor growth and immune evasion.[23,43] For example, in mouse models of chronic viral infection, IFNα exposure promoted myeloid-derived suppressor cell differentiation, which in turn inhibited $CD8^+$ T cell responses[44] or promoted cancer stem cell phenotypes in mouse models of fibrosarcoma.[45] On the other hand, enforced expression of IFNAR1 in $CD8^+$ T cells enhanced cytotoxic activity in subcutaneous MC38 mouse tumors,[46] or restoring IFNα signaling in cancer cells led to $CD8^+$ T cell-dependent therapeutic activity in distinct syngeneic and xenograft tumor mouse models.[24] In a similar way, depending on its target and the presence of other stimuli, IL-10 can either promote or inhibit tumor immunity. For example, by acting on DCs, IL-10 impairs activation and antigen presentation,[47] whereas at the same time, by impairing DC functions, IL-10 prevents DC-induced $CD8^+$ T cell apoptosis.[48] By acting on $CD8^+$ T cells, IL-10 prevents T cell exhaustion and promotes T cell invigoration in renal cell carcinoma patients and tumor mouse models.[49] However, combination of IFNα LV with IL-10 blockade did not affect liver metastasis growth. Further studies are necessary to understand how distinct combinations of cytokines reshape TME and immunity.

MHC-II-restricted antigen presentation may be necessary to maintain functional T cells in tumors,[50] and to enable response to immunotherapy.[51] In resistant mice, CTLA-4 may play a key role in reducing antigen presentation and T cell priming through CD80/CD86 sequestering, which in turn leads to defective T cell activation.[35] Indeed, CTLA-4 was highly upregulated in resistant mice in $CD8^+$ T cells as well as in *Eomes* $CD4^+$ T cells. Furthermore, we present evidence of positive correlations between the extent of IFNα signaling and, respectively, Tr1 signature score, *CTLA4* expression, and *HLA-C* expression in clinical samples of liver metastatic CRC, suggesting a mechanism of immune evasion in presence of IFNα common to both mouse and human. Together with other studies that have investigated the complexity of $CD4^+$ T cells in CRC liver metastases,[52] our findings uncover the potential relevance of regulatory T cell subpopulations, including Tr1, in thwarting immune control and establishing resistance to conventional immunotherapy. In agreement with this concept, combination of IFNα LV and CTLA-4 blockade resulted in a strong therapeutic effect, achieving complete regression of liver metastases in most mice.

Clinical development of the LV platform will leverage on the established clinical track record of *ex vivo* LV gene therapy in HSC and T cells and on the safety and efficacy of *in vivo* hepatocyte-directed LV gene transfer recently reported in non-human primates for the development of gene therapy for hemophilia.[15,53] Future successful translation of this strategy may help addressing a major unmet medical need of cancer patients suffering from metastatic liver disease.

Limitations of this study

Although our study is mostly limited to mouse models and thus suffers from their inherent limitations, several of our findings have clinical correlates supporting their relevance. In addition, albeit we found that IFNα released from engineered macrophages was well tolerated in mice, future clinical studies of our strategy would require additional preclinical toxicology and would start from a dose-escalating study to establish safe and tolerated doses and could benefit from the availability of therapeutic regimens alleviating any emerging IFNα-mediated toxicity and potentially disposing of the transduced liver macrophages.

STAR★METHODS

Detailed methods are provided in the online version of this paper and include the following:

- KEY RESOURCES TABLE
- RESOURCE AVAILABILITY
  - Lead contact
  - Materials availability
  - Data and code availability
- EXPERIMENTAL MODEL AND SUBJECT DETAILS
  - Mice
  - Cells
  - Human participants
- METHOD DETAILS
  - Plasmid design
  - Cell culture
  - LV production
  - LV copy number determination by ddPCR
  - Gene expression by ddPCR
  - Determination of KO of *Ifnar1* by ddPCR
  - FC analysis and fluorescence activated cell sorting
  - Mouse procedures
  - Monoclonal antibody injection

- Mouse experimental liver metastasis models
- Magnetic resonance imaging analysis for liver metastasis volume assessment
- Subcutaneous injection of MC38 cells
- Blood collection and analysis
- Processing of organs for FC analysis
- Processing of organs for imaging
- Single-cell RNA (scRNA) sequencing
- Spatial transcriptomic analysis
- Bulk RNA sequencing of samples from human liver metastases
- Nanostring analysis on patient metastases
- Statistical methods

SUPPLEMENTAL INFORMATION

Supplemental information can be found online at https://doi.org/10.1016/j.ccell.2023.09.014.

ACKNOWLEDGMENTS

We thank the IRCCS San Raffaele Hospital Flow Cytometry facility (FRACTAL), the IRCCS San Raffaele Center for Omics Sciences (COSR), the IRCCS San Raffaele Hospital Advanced Light and Electron Microscopy BioImaging Center (ALEMBIC), the San Raffaele Telethon Institute for Gene Therapy (SR-TIGET) Process Development Laboratory (PDL) for production of medium scale purified lentiviral vector stocks and the histopathology lab of the GLP facility of SR-TIGET for tissue processing. We acknowledge UTSW Microarray & Immune Phenotyping Core Facility for the quantification of autoreactive antibodies. We thank Eloise Scamardella, Carl Mirko Mercado, and Federica La Terza for technical support in confocal imaging acquisition and quantification, and Amleto Fiocchi for imaging of Visium slides. We thank Giulia Di Lullo for help on management of the clinical data. We thank Giovanni Sitia for providing *Ifnar1*$^{flox/flox}$ mice and Matteo Iannacone for providing *Cd4*^{Cre} mice. We also thank Silvia Gregori, Alessio Cantore, Anna Mondino and Chiara Bonini for scientific discussion and help with characterization of T cell populations. Graphical abstract and schematics were created with BioRender.com.

Funding: This work was supported by grants to: L.N. from the Italian Association for Cancer Research (AIRC) grant (“5 per Mille”, 22737 and IG, 20309); M.L.S. from the Lombardy Foundation for Biomedical Research (FRRB) “Early Career Award” grant (“GenTooControl”, ID 1751658), and the Cariplo Foundation grant (2019-1834).

AUTHOR CONTRIBUTIONS

T.K. and G.G. performed research, interpreted data, and wrote the manuscript.

S.B., M.G.S., C.B., G.T., and I.M. performed bioinformatic analyses.

C.B., M.N., and N.C. contributed to research and interpreted data.

T.C. performed MRI scans.

M.R. performed Nanostring analysis.

M.G. and R.O. contributed to single cell RNA sequencing.

A.K.R. supported PDL-grade lentiviral vector stock production.

M.O. helped establishing mouse liver metastasis models.

F.P., F.S., and C.D. performed histopathology analyses.

P.D. and L.A. contributed to human clinical data collection.

P.M.V.R. performed statistical analyses.

L.N. and M.L.S. designed the study, interpreted data, supervised research, wrote the manuscript and coordinated the work.

DECLARATION OF INTERESTS

L.N., M.L.S., and T.K. are inventors on a patent on KC-directed gene transfer and L.N. is an inventor on patents on miRNA-regulated LV technology filed and managed by the San Raffaele Scientific Institute and the Telethon Foundation.

INCLUSION AND DIVERSITY

We support inclusive, diverse, and equitable conduct of research.

Received: February 17, 2023
Revised: July 27, 2023
Accepted: September 27, 2023
Published: November 13, 2023

REFERENCES

1. Osterlund, P., Salminen, T., Soveri, L.M., Kallio, R., Kellokumpu, I., Lamminmäki, A., Halonen, P., Ristamäki, R., Lantto, E., Uutela, A., et al. (2021). Repeated centralized multidisciplinary team assessment of resectability, clinical behavior, and outcomes in 1086 Finnish metastatic colorectal cancer patients (RAXO): A nationwide prospective intervention study. Lancet Reg. Health. Eur. *3*, 100049.
2. Rhu, J., Heo, J.S., Choi, S.H., Choi, D.W., Kim, J.M., Joh, J.W., and Kwon, C.H.D. (2017). Streamline flow of the portal vein affects the lobar distribution of colorectal liver metastases and has a clinical impact on survival. Ann. Surg. Treat. Res. *92*, 348–354.
3. Robinson, M.W., Harmon, C., and O’Farrelly, C. (2016). Liver immunology and its role in inflammation and homeostasis. Cell. Mol. Immunol. *13*, 267–276.
4. Mittal, S.K., and Roche, P.A. (2015). Suppression of antigen presentation by IL-10. Curr. Opin. Immunol. *34*, 22–27.
5. Teratani, T., Mikami, Y., Nakamoto, N., Suzuki, T., Harada, Y., Okabayashi, K., Hagihara, Y., Taniki, N., Kohno, K., Shibata, S., et al. (2020). The liver-brain-gut neural arc maintains the T(reg) cell niche in the gut. Nature *585*, 591–596.
6. Lee, J.C., Mehdizadeh, S., Smith, J., Young, A., Mufazalov, I.A., Mowery, C.T., Daud, A., and Bluestone, J.A. (2020). Regulatory T cell control of systemic immunity and immunotherapy response in liver metastasis. Sci. Immunol. *5*, eaba0759.
7. Bonnal, R.J.P., Rossetti, G., Lugli, E., De Simone, M., Gruarin, P., Brummelman, J., Drufuca, L., Passaro, M., Bason, R., Gervasoni, F., et al. (2021). Clonally expanded EOMES(+) Tr1-like cells in primary and metastatic tumors are associated with disease progression. Nat. Immunol. *22*, 735–745.
8. Yu, J., Green, M.D., Li, S., Sun, Y., Journey, S.N., Choi, J.E., Rizvi, S.M., Qin, A., Waninger, J.J., Lang, X., et al. (2021). Liver metastasis restrains immunotherapy efficacy via macrophage-mediated T cell elimination. Nat. Med. *27*, 152–164.
9. Le, D.T., Durham, J.N., Smith, K.N., Wang, H., Bartlett, B.R., Aulakh, L.K., Lu, S., Kemberling, H., Wilt, C., Luber, B.S., et al. (2017). Mismatch repair deficiency predicts response of solid tumors to PD-1 blockade. Science *357*, 409–413.
10. Wang, X., Ji, Q., Yan, X., Lian, B., Si, L., Chi, Z., Sheng, X., Kong, Y., Mao, L., Bai, X., et al. (2020). The Impact of Liver Metastasis on Anti-PD-1 Monoclonal Antibody Monotherapy in Advanced Melanoma: Analysis of Five Clinical Studies. Front. Oncol. *10*, 546604.
11. Correia, A.L. (2023). Locally sourced: site-specific immune barriers to metastasis. Nat. Rev. Immunol. *23*, 522–538.
12. Lutz, E.A., Agarwal, Y., Momin, N., Cowles, S.C., Palmeri, J.R., Duong, E., Hornet, V., Sheen, A., Lax, B.M., Rothschilds, A.M., et al. (2022). Alum-anchored intratumoral retention improves the tolerability and antitumor efficacy of type I interferon therapies. Proc. Natl. Acad. Sci. USA *119*, e2205983119.
13. Crockett, D.M., McCabe, B.F., Lusk, R.P., and Mixon, J.H. (1987). Side effects and toxicity of interferon in the treatment of recurrent respiratory papillomatosis. Ann. Otol. Rhinol. Laryngol. *96*, 601–607.

14. Sleijfer, S., Bannink, M., Van Gool, A.R., Kruit, W.H.J., and Stoter, G. (2005). Side effects of interferon-alpha therapy. Pharm. World Sci. *27*, 423–431.

15. Milani, M., Annoni, A., Moalli, F., Liu, T., Cesana, D., Calabria, A., Bartolaccini, S., Biffi, M., Russo, F., Visigalli, I., et al. (2019). Phagocytosis-shielded lentiviral vectors improve liver gene therapy in nonhuman primates. Sci. Transl. Med. *11*, eaav7325.

16. Peng, K.W., Pham, L., Ye, H., Zufferey, R., Trono, D., Cosset, F.L., and Russell, S.J. (2001). Organ distribution of gene expression after intravenous infusion of targeted and untargeted lentiviral vectors. Gene Ther. *8*, 1456–1463.

17. Tao, N., Gao, G.P., Parr, M., Johnston, J., Baradet, T., Wilson, J.M., Barsoum, J., and Fawell, S.E. (2001). Sequestration of adenoviral vector by Kupffer cells leads to a nonlinear dose response of transduction in liver. Mol. Ther. *3*, 28–35.

18. Cantore, A., and Naldini, L. (2021). WFH State-of-the-art paper 2020: In vivo lentiviral vector gene therapy for haemophilia. Haemophilia *27* (*Suppl 3*), 122–125.

19. Squadrito, M.L., Pucci, F., Magri, L., Moi, D., Gilfillan, G.D., Ranghetti, A., Casazza, A., Mazzone, M., Lyle, R., Naldini, L., and De Palma, M. (2012). miR-511-3p modulates genetic programs of tumor-associated macrophages. Cell Rep. *1*, 141–154.

20. Sakai, E., Nakayama, M., Oshima, H., Kouyama, Y., Niida, A., Fujii, S., Ochiai, A., Nakayama, K.I., Mimori, K., Suzuki, Y., et al. (2018). Combined Mutation of Apc, Kras, and Tgfbr2 Effectively Drives Metastasis of Intestinal Cancer. Cancer Res. *78*, 1334–1346.

21. Soldi, M., Sergi Sergi, L., Unali, G., Kerzel, T., Cuccovillo, I., Capasso, P., Annoni, A., Biffi, M., Rancoita, P.M.V., Cantore, A., et al. (2020). Laboratory-Scale Lentiviral Vector Production and Purification for Enhanced Ex Vivo and In Vivo Genetic Engineering. Mol. Ther. Methods Clin. Dev. *19*, 411–425.

22. Yofe, I., Landsberger, T., Yalin, A., Solomon, I., Costoya, C., Demane, D.F., Shah, M., David, E., Borenstein, C., Barboy, O., et al. (2022). Anti-CTLA-4 antibodies drive myeloid activation and reprogram the tumor microenvironment through FcgammaR engagement and type I interferon signaling. Nat. Can. (Ott.) *3*, 1336–1350.

23. Boukhaled, G.M., Harding, S., and Brooks, D.G. (2021). Opposing Roles of Type I Interferons in Cancer Immunity. Annu. Rev. Pathol. *16*, 167–198.

24. Gozgit, J.M., Vasbinder, M.M., Abo, R.P., Kunii, K., Kuplast-Barr, K.G., Gui, B., Lu, A.Z., Molina, J.R., Minissale, E., Swinger, K.K., et al. (2021). PARP7 negatively regulates the type I interferon response in cancer cells and its inhibition triggers antitumor immunity. Cancer Cell *39*, 1214–1226.e10.

25. Tran, N.L., Ferreira, L.M., Alvarez-Moya, B., Buttiglione, V., Ferrini, B., Zordan, P., Monestiroli, A., Fagioli, C., Bezzecchi, E., Scotti, G.M., et al. (2022). Continuous sensing of IFNalpha by hepatic endothelial cells shapes a vascular antimetastatic barrier. Elife *11*, e80690.

26. Hingorani, S.R., Wang, L., Multani, A.S., Combs, C., Deramaudt, T.B., Hruban, R.H., Rustgi, A.K., Chang, S., and Tuveson, D.A. (2005). Trp53R172H and KrasG12D cooperate to promote chromosomal instability and widely metastatic pancreatic ductal adenocarcinoma in mice. Cancer Cell *7*, 469–483.

27. Roncarolo, M.G., Gregori, S., Bacchetta, R., Battaglia, M., and Gagliani, N. (2018). The Biology of T Regulatory Type 1 Cells and Their Therapeutic Application in Immune-Mediated Diseases. Immunity *49*, 1004–1019.

28. Kim, H.D., Jeong, S., Park, S., Lee, Y.J., Ju, Y.S., Kim, D., Song, G.W., Lee, J.H., Kim, S.Y., Shin, J., et al. (2021). Implication of CD69(+) CD103(+) tissue-resident-like CD8(+) T cells as a potential immunotherapeutic target for cholangiocarcinoma. Liver Int. *41*, 764–776.

29. Gagliani, N., Magnani, C.F., Huber, S., Gianolini, M.E., Pala, M., Licona-Limon, P., Guo, B., Herbert, D.R., Bulfone, A., Trentini, F., et al. (2013). Coexpression of CD49b and LAG-3 identifies human and mouse T regulatory type 1 cells. Nat. Med. *19*, 739–746.

30. Brockmann, L., Gagliani, N., Steglich, B., Giannou, A.D., Kempski, J., Pelczar, P., Geffken, M., Mfarrej, B., Huber, F., Herkel, J., et al. (2017). IL-10 Receptor Signaling Is Essential for TR1 Cell Function In Vivo. J. Immunol. *198*, 1130–1141.

31. Roncarolo, M.G., Gregori, S., Battaglia, M., Bacchetta, R., Fleischhauer, K., and Levings, M.K. (2006). Interleukin-10-secreting type 1 regulatory T cells in rodents and humans. Immunol. Rev. *212*, 28–50.

32. Magnani, C.F., Alberigo, G., Bacchetta, R., Serafini, G., Andreani, M., Roncarolo, M.G., and Gregori, S. (2011). Killing of myeloid APCs via HLA class I, CD2 and CD226 defines a novel mechanism of suppression by human Tr1 cells. Eur. J. Immunol. *41*, 1652–1662.

33. Pedroza-Gonzalez, A., Zhou, G., Vargas-Mendez, E., Boor, P.P., Mancham, S., Verhoef, C., Polak, W.G., Grünhagen, D., Pan, Q., Janssen, H.L., et al. (2015). Tumor-infiltrating plasmacytoid dendritic cells promote immunosuppression by Tr1 cells in human liver tumors. OncoImmunology *4*, e1008355.

34. Chen, P.P., Cepika, A.M., Agarwal-Hashmi, R., Saini, G., Uyeda, M.J., Louis, D.M., Cieniewicz, B., Narula, M., Amaya Hernandez, L.C., Harre, N., et al. (2021). Alloantigen-specific type 1 regulatory T cells suppress through CTLA-4 and PD-1 pathways and persist long-term in patients. Sci. Transl. Med. *13*, eabf5264.

35. Topalian, S.L., Drake, C.G., and Pardoll, D.M. (2015). Immune checkpoint blockade: a common denominator approach to cancer therapy. Cancer Cell *27*, 450–461.

36. Hanada, K.I., Zhao, C., Gil-Hoyos, R., Gartner, J.J., Chow-Parmer, C., Lowery, F.J., Krishna, S., Prickett, T.D., Kivitz, S., Parkhurst, M.R., et al. (2022). A phenotypic signature that identifies neoantigen-reactive T cells in fresh human lung cancers. Cancer Cell *40*, 479–493.e6.

37. Zhang, W., Zhangyuan, G., Wang, F., Jin, K., Shen, H., Zhang, L., Yuan, X., Wang, J., Zhang, H., Yu, W., et al. (2021). The zinc finger protein Miz1 suppresses liver tumorigenesis by restricting hepatocyte-driven macrophage activation and inflammation. Immunity *54*, 1168–1185.e8.

38. Li, A.W., and Lim, W.A. (2020). Engineering cytokines and cytokine circuits. Science *370*, 1034–1035.

39. Hickerson, B.T., Sefing, E.J., Bailey, K.W., Van Wettere, A.J., Penichet, M.L., and Gowen, B.B. (2020). Type I interferon underlies severe disease associated with Junin virus infection in mice. Elife *9*, e55352.

40. Bondet, V., Rodero, M.P., Posseme, C., Bost, P., Decalf, J., Haljasmägi, L., Bekaddour, N., Rice, G.I., Upasani, V., Herbeuval, J.P., et al. (2021). Differential levels of IFNalpha subtypes in autoimmunity and viral infection. Cytokine *144*, 155533.

41. Wanisch, K., and Yáñez-Muñoz, R.J. (2009). Integration-deficient lentiviral vectors: a slow coming of age. Mol. Ther. *17*, 1316–1332.

42. Levings, M.K., Sangregorio, R., Galbiati, F., Squadrone, S., de Waal Malefyt, R., and Roncarolo, M.G. (2001). IFN-alpha and IL-10 induce the differentiation of human type 1 T regulatory cells. J. Immunol. *166*, 5530–5539.

43. Dickow, J., Francois, S., Kaiserling, R.L., Malyshkina, A., Drexler, I., Westendorf, A.M., Lang, K.S., Santiago, M.L., Dittmer, U., and Sutter, K. (2019). Diverse Immunomodulatory Effects of Individual IFNalpha Subtypes on Virus-Specific CD8(+) T Cell Responses. Front. Immunol. *10*, 2255.

44. Taleb, K., Auffray, C., Villefroy, P., Pereira, A., Hosmalin, A., Gaudry, M., and Le Bon, A. (2017). Chronic Type I IFN Is Sufficient To Promote Immunosuppression through Accumulation of Myeloid-Derived Suppressor Cells. J. Immunol. *198*, 1156–1163.

45. Musella, M., Guarracino, A., Manduca, N., Galassi, C., Ruggiero, E., Potenza, A., Maccafeo, E., Manic, G., Mattiello, L., Soliman Abdel Rehim, S., et al. (2022). Type I IFNs promote cancer cell stemness by triggering the epigenetic regulator KDM1B. Nat. Immunol. *23*, 1379–1392.

46. Katlinski, K.V., Gui, J., Katlinskaya, Y.V., Ortiz, A., Chakraborty, R., Bhattacharya, S., Carbone, C.J., Beiting, D.P., Girondo, M.A., Peck, A.R., et al. (2017). Inactivation of Interferon Receptor Promotes the

Establishment of Immune Privileged Tumor Microenvironment. Cancer Cell *31*, 194–207.

47. Schülke, S. (2018). Induction of Interleukin-10 Producing Dendritic Cells As a Tool to Suppress Allergen-Specific T Helper 2 Responses. Front. Immunol. *9*, 455.
48. Qiao, J., Liu, Z., Dong, C., Luan, Y., Zhang, A., Moore, C., Fu, K., Peng, J., Wang, Y., Ren, Z., et al. (2019). Targeting Tumors with IL-10 Prevents Dendritic Cell-Mediated CD8(+) T Cell Apoptosis. Cancer Cell *35*, 901–915.e4.
49. Naing, A., Infante, J.R., Papadopoulos, K.P., Chan, I.H., Shen, C., Ratti, N.P., Rojo, B., Autio, K.A., Wong, D.J., Patel, M.R., et al. (2018). PEGylated IL-10 (Pegilodecakin) Induces Systemic Immune Activation, CD8(+) T Cell Invigoration and Polyclonal T Cell Expansion in Cancer Patients. Cancer Cell *34*, 775–791.e3.
50. Kilian, M., Sheinin, R., Tan, C.L., Friedrich, M., Krämer, C., Kaminitz, A., Sanghvi, K., Lindner, K., Chih, Y.C., Cichon, F., et al. (2023). MHC class II-restricted antigen presentation is required to prevent dysfunction of cytotoxic T cells by blood-borne myeloids in brain tumors. Cancer Cell *41*, 235–251.e9.
51. Lester, D.K., Burton, C., Gardner, A., Innamarato, P., Kodumudi, K., Liu, Q., Adhikari, E., Ming, Q., Williamson, D.B., Frederick, D.T., et al. (2023). Fucosylation of HLA-DRB1 regulates CD4(+) T cell-mediated anti-melanoma immunity and enhances immunotherapy efficacy. Nat. Can. (Ott.) *4*, 222–239.
52. Liu, Y., Zhang, Q., Xing, B., Luo, N., Gao, R., Yu, K., Hu, X., Bu, Z., Peng, J., Ren, X., and Zhang, Z. (2022). Immune phenotypic linkage between colorectal cancer and liver metastasis. Cancer Cell *40*, 424–437.e5.
53. Milani, M., Canepari, C., Liu, T., Biffi, M., Russo, F., Plati, T., Curto, R., Patarroyo-White, S., Drager, D., Visigalli, I., et al. (2022). Liver-directed lentiviral gene therapy corrects hemophilia A mice and achieves normal-range factor VIII activity in non-human primates. Nat. Commun. *13*, 2454.
54. Squadrito, M.L., Cianciaruso, C., Hansen, S.K., and De Palma, M. (2018). EVIR: chimeric receptors that enhance dendritic cell cross-dressing with tumor antigens. Nat. Methods *15*, 183–186.
55. Brown, B.D., Gentner, B., Cantore, A., Colleoni, S., Amendola, M., Zingale, A., Baccarini, A., Lazzari, G., Galli, C., and Naldini, L. (2007). Endogenous microRNA can be broadly exploited to regulate transgene expression according to tissue, lineage and differentiation state. Nat. Biotechnol. *25*, 1457–1467.
56. Cilenti, F., Barbiera, G., Caronni, N., Iodice, D., Montaldo, E., Barresi, S., Lusito, E., Cuzzola, V., Vittoria, F.M., Mezzanzanica, L., et al. (2021). A PGE(2)-MEF2A axis enables context-dependent control of inflammatory gene expression. Immunity *54*, 1665–1682.e14.
57. Wherry, E.J., Ha, S.J., Kaech, S.M., Haining, W.N., Sarkar, S., Kalia, V., Subramaniam, S., Blattman, J.N., Barber, D.L., and Ahmed, R. (2007). Molecular signature of CD8+ T cell exhaustion during chronic viral infection. Immunity *27*, 670–684.
58. Potenza, A., Balestrieri, C., Spiga, M., Albarello, L., Pedica, F., Manfredi, F., Cianciotti, B.C., De Lalla, C., Botrugno, O.A., Faccani, C., et al. (2023). Revealing and harnessing CD39 for the treatment of colorectal cancer and liver metastases by engineered T cells. Gut *72*, 1887–1903.

STAR★METHODS

KEY RESOURCES TABLE

REAGENT or RESOURCE	SOURCE	IDENTIFIER
Antibodies		
Rat anti-CD11b (M1/70)	Biolegend	101242
Hamster anti-CD11c (N418)	Biolegend	117318
Rat anti-MRC1 (C068C2)	BD Bioscience	141712
Mouse anti-dINGFR (ME20.4-1.H4)	Miltenyi	130-113-418
Rat anti-PDL1 (10F.9G2)	Biolegend	124308
Rat anti-PD1 (29F.1A12)	Biolegend	135216
Rat anti-CD4 (RM4-5)	BD Bioscience	564933
Rat anti-CD44 (IM7)	BD Bioscience	563058
Rat anti-CD45 (30-F11)	Biolegend	103138
Rat anti-B220 (RA3-6B2)	Biolegend	103224
Rat anti-B220 (RA3-6B2)	BD Bioscience	553090; 558108
Rat anti-CD86 (GL-1)	Biolegend	105030
Rat anti-CD8a (53-6.7)	BD Bioscience	553030
Mouse pentamer-SIINFEKL	Proimmune	F093-4C
Rat anti-F4/80 (BM8)	Biolegend	123128; 123108; 123110
Rat anti-Ly6c (HK1.4)	eBioscience	48-5932-82
Rat anti-Ly6c (HK1.4)	Biolegend	128026
Rat anti-Ly6g (1A8)	Biolegend	127618
Rat anti-GR1 (RB6-8C5)	BD Bioscience	553129
Rat anti-Ly6g (1A8)	Biosciences	563005; 741813
Hamster anti-TCRb (H57-597)	Biosciences	563135
Rat anti-CD3 (17A2)	Biolegend	100206
Rat anti-EOMES (W17001A)	Biolegend	157706
Mouse anti-TBET (4B10)	Biolegend	644835
Chicken anti-GFP (Polyclonal)	Abcam	Ab13970
Goat anti-CLEC4F (Polyclonal)	Thermo Fisher	PA547396
Rat anti-F4/80 (C1-A3-1)	Abcam	ab6640
Goat anti-VSIG4 (Polyclonal)	R&D Systems	AF4674
Rabbit anti-mCherry (Polyclonal)	Abcam	ab167453
Goat anti-E-Cadherin (Polyclonal)	R&D Systems	AF748
Rabbit anti-CD11c (Polyclonal)	Cell Signaling	97585S
Rabbit anti-CD31 (Polyclonal)	Abcam	ab28364
Mouse anti-a-SMA (1A4)	Merck	C6198-.2ML
Rabbit anti-CD4 (EPR19514)	Abcam	ab183685
Rat anti-CD8a (4SM16)	eBioscience	14-019-582
Donkey anti-Chicken (Polyclonal)	Jackson	703-545-155
Donkey anti-Goat (Polyclonal)	Invitrogen	A31573
Donkey anti-Rat (Polyclonal)	Abcam	Ab150154
Goat anti-Chicken (Polyclonal)	Invitrogen	A-11039
Goat anti-Rat (Polyclonal)	Invitrogen	A21247
Goat anti-Rabbit (Polyclonal)	Invitrogen	A11010
Donkey anti-Chicken (Polyclonal)	Jackson Immuno Research	703-545-155
Donkey anti-Rat (Polyclonal)	Invitrogen	A32849
Donkey anti-Goat (Polyclonal)	Invitrogen	A32849

(*Continued on next page*)

Continued

REAGENT or RESOURCE	SOURCE	IDENTIFIER
Donkey anti-Rabbit (Polyclonal)	Invitrogen	A11010
Rat anti-Mouse Fc Block	BD Biosciences	553142
Mouse anti-LAG3 (874512)	RnD Systems	#Mab23196
Rabbit anti-CD4 (SP35)	Roche-Ventana	5552737001
Rabbit anti-CD4 (D7D2Z)	Cell Signaling Technology	25229
Mouse anti-CTLA4 (OTI1G10)	Origene	TA810299
Rabbit anti-EOMES (EPR19012)	Abcam	183991
Donkey anti-mouse (Polyclonal)	Abcam	ab150105
Rat anti-IL-10R (1B1.3A)	BioXCell	BE0050
Rat IgG1k anti-HRP (HRPN)	BioXCell	BE0088
Siriam Hamster anti-mouse CTLA4 (9H10)	BioXCell	BE0131
Siriam Hamster Isotype control	BioXCell	BE0087
Rat anti-mouse CD8a (53-6.7)	BioXCell	BE0004-1
Rat IgG2a anti-trinitrophenol (2A3)	BioXCell	BE0089
Experimental models: Organisms/strains		
NSG	Charles River Laboratory	#614
C57BL/6	Charles River Laboratory	#027
Nude (NU/NUCD)	Charles River Laboratory	#086
B6.Cg-Tg(Cd4-cre)1Cwi/BfluJ	The Jackson Laboratory	#022071
B6(Cg)-*Ifnar1*$^{tm1.1Ees}$/J	The Jackson Laboratory	#028256
Experimental models: Cell lines		
Human: HEK293T	ATCC	Cat# CRL-3216
Mouse: BMDMs	NA	NA
Mouse: MC38	Provided by Amgen	NA
Mouse: K8484	Hingorani et al., 2005[26]	NA
Mouse: AKTPF	Sakai et al., 2018[20]	NA
Deposited data		
scRNA and spatial transcriptomics sequencing data	This paper	GSE221360
Bulk RNA sequencing data	This paper; Potenza et al., 2023[58]	GSE200133
Software and algorithms		
R 3.6.2	http://www.R-project.org/	NA
Prism 9 Version 9.3.1	https://www.graphpad.com	NA
FlowJo version 10.8.1	https://www.flowjo.com/	NA
FCS Express Version 7.12.0007	https://denovosoftware.com/	NA
QuantaSoft software (Biorad) Version 1.7	https://www.bio-rad.com/	NA
MIPAV Version 11.0.7	https://mipav.cit.nih.gov/	NA
Fiji - ImageJ2 version 2.3.0/1.53q	https://fiji.sc/	NA
Code	This paper	http://www.bioinfotiget.it/gitlab/custom/squadrito_livertumor2022
Other		
TACTGACGCTCTCGACC	ThermoFisher	NA
TCTCGACGCAGGACTCG	ThermoFisher	NA
5′-(FAM)-ATCTCTCTCCTTCTAGCCTC-(MGB)-3′	ThermoFisher	NA
ACCGATTCCAGATGATTGGC	ThermoFisher	NA
TCCATATTAATGCAGTGCTTG	ThermoFisher	NA
5′-(HEX)-AGAGGCCTGTCCTGCAGCTCATGG –(BHQ-1)- 3′	ThermoFisher	NA
Hprt TaqManTM Gene Expression Assay	Invitrogen	Mm03024075_m1
Irf7 TaqManTM Gene Expression Assay	Invitrogen	Mm00516788_m1
Ifit1 TaqManTM Gene Expression Assay	Invitrogen	Mm00515153_m1

(*Continued on next page*)

Continued

REAGENT or RESOURCE	SOURCE	IDENTIFIER
Oas1a TaqManTM Gene Expression Assay	Invitrogen	Mm00836412_m1
GAPDH TaqManTM Gene Expression Assay	Invitrogen	Hs00894322_cn

RESOURCE AVAILABILITY

Lead contact

Further information and requests for resources and reagents should be directed to and will be fulfilled by the lead contact, Mario Leonardo Squadrito (squadrito.mario@hsr.it).

Materials availability

All unique reagents generated in this study are available from the lead contact with a completed Materials Transfer Agreement.

Data and code availability

- Bulk RNA and scRNA sequencing data have been deposited at GEO and are publicly available as of the date of publication. Accession numbers are listed in the key resources table.
- All original code is publicly available. Accession links are available in the key resources table.
- Any additional information required to reanalyze the data reported in this paper is available from the lead contact upon request.

EXPERIMENTAL MODEL AND SUBJECT DETAILS

Mice

In this study, we employed male or female C57Bl/6N mice (in all experiments performed using IFNα LV or Control LV), NUDE mice (if not indicated differently, in all experiments using *Mrc1*.GFP LV or *Mrc1*.GFP.miRT LV) or NSG mice that were purchased from Charles River Laboratory. IFNAR1$^{flox/flox}$ and CD4^{Cre} mice were provided by Giovanni Sitia and Matteo Iannacone, respectively. They were crossed to obtain homozygous mice carrying both genetic modifications. All experiments and procedures were performed according to protocols approved by the Institutional Animal Care and Use Committee (IACUC) at San Raffaele Hospital animal facilities (IACUC number: 1007, 1098, 1108, 1227 and 1383) and authorized by the Italian Ministry of Health and local authorities according to the Italian law. Mice were used between 6 and 8 weeks of age and were maintained in Specific Pathogen-free (SPF) animal research facilities with a 12h/12h dark/light cycle and standardized temperature (22 +/- 2°C) and humidity (55 +/- 5%).

Cells

HEK293T were employed to produce and titer LVs. These cells were purchased from ATCC and their authenticity is supported by their capability to produce high titer LV stocks. MC38 cells were used to mimic CRC liver metastasis upon liver implantation. MC38 were obtained from Amgen. AKTPF cells were obtained from the laboratory of Masanobu Oshima. Their authenticity is supported by their capability to produce liver metastases that histologically recapitulate the human disease. K8484 are available and routinely used in our institute. The cells were used to mimic PDAC liver metastases. Primary BMDMs were obtained from C57BL6 mice, used protocols described below.

Human participants

All participants were patients at San Raffaele Hospital, Milan, Italy. The study was approved by the ethical committee of the institute and samples were collected upon written informed consent. No distinction between sex, ancestry, socio-economical status, age or ethnicity was made during recruitment of patients. Peri-metastatic and metastatic liver samples were collected upon surgery. Clinical trial protocol, data collection and study design were deposited in ClinicalTrials.gov with the identifier number ctgov:NCT04622423 and can be retrieved at https://clinicaltrials.gov/ct2/show/NCT04622423?cond=NCT04622423&draw=2&rank=1.

METHOD DETAILS

Plasmid design

To originate the *Mrc1*.GFP lentiviral vector (LV), we inserted a putative *Mrc1* promoter sequence encompassing a 1883 bp DNA sequence (MM39 assembly: CHR2:14232425-14234307) into a previously described *PGK*.GFP LV[54] by replacing the PGK promoter sequence by using the restriction enzyme sites XhoI and AgeI. The bidirectional miRT LVs were generated by inserting four tandem copies with perfect complementarity to miR-122-5p (miRT-122-5p: 5′- ACAAACACCATTGTCACACTCCA -3′) or to miR-126-3p (miRT-126-3p: 5′- CGCATTATTACTCACGGTACGA -3′) with randomized 4 bp DNA linker sequences separating the miRT sites. The 4 copies of the miRT sequences were then inserted downstream of the WPRE sequence of a bidirectional LV[55] containing a minimal cytomegalovirus (mCMV) and a human phosphoglycerate kinase 1 (*PGK*) promoter located in opposite direction and driving the

expression of a truncated low affinity nerve growth factor receptor (dlNGFR) and GFP respectively. The miRTs were inserted by employing the restriction enzyme site KpnI. The *Mrc1*.GFP.miRT LV was originated by inserting 4 copies of the miRT-122-5p and 4 of the miRT-126-3p downstream of the WPRE in the *Mrc1*.GFP LV transfer vector plasmid by using the restriction enzyme site KpnI. The IFNα LV transfer vector plasmid was created by replacing the GFP sequence of the *Mrc1*.GFP.miRT LV transfer vector plasmid with a cDNA encoding for the murine IFNα1 protein by using the restriction enzyme sites SalI and ScaI. The Control LV was generated by depleting the GFP sequence of the *Mrc1*.GFP LV transfer vector plasmid by digesting with the restriction enzymes AgeI and SalI, followed by insertion of 4 copies of miRT-122-5p and 4 copies of miRT-126-3p downstream of the WPRE by using the restriction enzyme site KpnI.

Cell culture

HEK293T, MC38 and K8484 cells were cultured in adherent cell culture plates in Iscove's Modification of Dulbecco's Modified Eagle Medium (IMDM, Corning) supplemented with 10% fetal bovine serum (FBS; HyClone™), penicillin (100 IU/mL) and streptomycin (100 μg/mL). For generation of the MC38 cells expressing mCherry (MC38-mCherry) in virtually all cells (99.97% of all cells), MC38 cells were transduced with a LV driving the expression of a chimeric protein formed by mCherry fused to the C terminus of the CD81 transmembrane domain from a constitutively expressed human phosphoglycerate kinase 1 (PGK) promoter. For generation of and MC38-OVA cells, MC38 cells were transduced with an LV driving the expression of full-length chicken ovalbumin (OVA) from a hPGK promoter and a VCN of 2.86 was detected in MC38-OVA cells.

AKTPF-organoids were cultured at 37°C in 30 μL of phenol-red free and growth factor reduced matrigel (BD Biosciences) in a 48-well surrounded by 300 μL Advanced Dulbecco's Modified Eagle Medium (DMEM)/F-12 medium (Thermo Fisher Scientific) supplemented with 2 % GlutaMAX™ supplement (Gibco), penicillin (100 IU/mL), streptomycin (100 μg/mL), 1 % hepes buffer solution (Gibco), 1 % N-2 supplement (Gibco), 2 % B-27 supplement (Gibco), 1 mM N-acetylcysteine- (Sigma-Aldrich) and 50 ng/mL murine epidermal growth factor (rmEGF; Gibco). To convert the AKTPF organoids into an adherent 2D cell culture, AKTPF organoids were passed two times through NSG mice and once through c57Bl6 mice. For that purpose, AKTPF organoids were transplanted into NSG mice through intrasplenic injection and recovered after four weeks. Single cells were obtained by cutting the tumor into small pieces and filtering through a 45 μm cell strainer. Then, 1,000,000 single cells were transplanted into NSG mice by intrasplenic injection. After recovery of the tumor cells, 4 weeks after tumor transplant, tumor cells were cultured in cell culture-treated plates using DMEM/F-12 medium supplemented with 10 % FBS, 2 % GlutaMAX™, penicillin (100 IU/mL) and streptomycin (100 μg/mL). After *in vitro* culture, 1,000,000 tumor cells were transplanted into c57Bl6 mice. Four weeks after transplant tumor cells were retrieved and put in culture as described previously. Resulting cells were culture as described above and used in experiments employing AKTPF cells.

For retrieval of bone marrow-derived macrophages (BMDMs), bone marrow was harvested from C57Bl6 mice by flushing the femur and tibia with 10 mL MACS buffer (Miltenyi Biotec). For red blood cell lysis, 1 mL of desalt water was added to the cell pellet and immediately afterwards 50 mL MACS buffer were added. Cells were cultured in macrophage culture medium composed of RPMI medium (Corning) supplemented with 10 % FBS, 2 % GlutaMAX™ Supplement (Gibco), penicillin (100 IU/mL), streptomycin (100 μg/mL) and 100 ng/mL of mouse M-CSF (Miltenyi Biotec).

After seven days, 1,000,000 BMDMs were seeded into a 24 well plate and transduced with LVs at an MOI of 10. The following day macrophage culture medium was added to the cells. We added to the cell culture medium either, for M2-like polarization, 50 ng/mL of mouse IL-4 (Miltenyi) or, for M1-like polarization, 100 ng of lipopolysaccharides (LPS) from Escherichia coli O55:B5 (Sigma-Aldrich) and 5 ng/mL of mouse IFNγ (Miltenyi). Six days after induction of polarization, flow cytometry (FC) analysis was performed.

LV production

In this study, third generation VSV-G pseudotyped LVs were used. LV stocks were either produced in laboratory grade or process development laboratory (PDL) grade, as described previously.[21] For the biodistribution study in in presence of AKTPF derived liver metastases, CD47 depleted LVs were produced in CD47-negative HEK 293T cells as described previously.[15] The titer of the LV stocks was measured in HEK 293T cell-transducing units (TU/mL), as described previously.[21]

LV copy number determination by ddPCR

From cell culture samples genomic DNA was extracted by using the Maxwell® 16 instrument (Promega) with Maxwell® 16 DNA purification kits (Promega). Genomic DNA from whole tissue samples was extracted by using the DNeasy Blood and Tissue Kit (Qiagen). LV copy number was determined using a QX200 Droplet Digital PCR System (Biorad) apparatus. The digital droplet PCR was performed according to manufacturer's instructions; briefly 5-20 ng of genomic DNA was added to the reaction, primers were used at a concentration of 900 nM and the detection probes at 250 nM. Droplet quantification was acquired using the BioRad QX200 Droplet Reader and analysed by using the QuantaSoft software (Biorad). For the detection of HIV genomes, the following primer and probe set was used: forward primer: 5′-TACTGACGCTCTCGACC -3′; reverse primer: 5′-TCTCGACGCAGGACTCG -3′; probe in the FAM detection channel: 5′-(FAM)-ATCTCTCTCCTTCTAGCCTC-(MGB)-3′. As normalizer for murine samples the *Sema3a* gene was used: forward primer: 5′-ACCGATTCCAGATGATTGGC -3′; reverse primer: 5′-TCCATATTAATGCAGTGCTTG -3′; detection probe in Hex channel: 5′-(HEX)-AGAGGCCTGTCCTGCAGCTCATGG –(BHQ-1)- 3′. As normalizer for human samples, a commercially available

GAPDH expression assay was used (TaqMan™ Gene Expression Assay, Invitrogen; Hs00894322_cn). LV copies per genome were calculated by the formula:

$$\text{LV copies per genome} = \frac{concentration(HIV)}{concentration(Normalizer)} * 2$$

Gene expression by ddPCR

For gene expression analysis, RNA was extracted from frozen tissue using the RNeasy® Plus Mini Kit (Qiagen). Retrotranscription was performed according to manufacturer's instruction by using the SuperScriptTM IV VILO (Invitrogen). Five-20 ng of cDNA were used as input for the gene expression analysis. TaqMan™ Gene Expression Assays from Invitrogen are described in the key resources table.

Data acquisition using ddPCR and analysis were performed as described for LV copy number determination (above).

Determination of KO of *Ifnar1* by ddPCR

To determine knock out of *Ifnar1* from target cell populations, $CD4^+$ T cells, $CD8^+$ T cells, B cells and $CD11b^+$ cells were sorted by flow-cytometry activated cell sorting from blood. Genomic DNA was extracted using the QIAamp DNA Micro kit (Qiagen). ddPCR by employing Eva Green (Biorad) was performed on the genomic DNA with primers amplifying *Ifnar1* and *Sema3a loci*. Two ng of genomic DNA were used, primers were used at a concentration of 100 μM. For *Sema3a*, the following primers were used: forward primer: 5′-ACCGATTCCAGATGATTGGC -3′; reverse primer: 5′-TCCATATTAATGCAGTGCTTG -3′. For *Ifnar1*, the primers used were: forward primer: 5′-ACTCAGGTTCGCTCCATCAG-3′; reverse primer: 5′-CTTTTAACCACTTCGCCTCGT-3′. Droplet quantification was acquired using the BioRad QX200 Droplet Reader and analysed by using the QuantaSoft software (Biorad).

FC analysis and fluorescence activated cell sorting

Viability of cells was assessed by using either 7AAD nuclear staining or LIVE/DEAD™ Fixable Blue Dead Cell Stain Kit (Invitrogen) according to manufacturer's recommendation for fixed samples. Upon single cell dissociation (see below), to prevent unspecific staining through binding of the FC receptor, we added to the cells Fc Block (BD Pharmagen). For membrane bound antigens, samples were stained for 15 minutes on ice. For staining of intracellular proteins, cells were fixed, permeabilized and stained using the True-Nuclear™ Transcription Factor Buffer Set (BioLegend) according to manufacturer's recommendation. For the staining of TCRs specific for the SIINFEKL peptide loaded on MHC class I (H2-Kb), samples were stained with an SIINFEKL-loaded MHC class I pentamer (ProImmune) according to manufacturer's instruction. We used the following gating strategy to define cell populations by flow cytometry: B cells ($CD45^+$ $B220^+$), $CD4^+$ T cells ($CD45^+$ $CD4^+$), $CD45^-$ cells in the bone marrow ($CD45^-$), $CD8^+$ T cells in the tumor ($CD45^+$ $TCRb^+$ $CD8^+$), $CD8^+$ T cells in the blood ($CD45^+$ $B220^-$ $CD8^+$), $CD86^+$ TAMs ($CD45^+$ $CD11b^+$ $F4/80^+$ $CD86^+$), DCs in the liver ($CD45^+$ $F4/80^-$ $CD11c^{high}$), $EOMES^+$ CD4 T cells in the tumor ($CD45^+$ $B220^-$ $CD11b^-$ $CD4^+$ $EOMES^+$), granulocytes ($CD45^+$ $B220^-$ $Ly6g^+$), inflammatory monocytes in the blood ($CD45^+$ $CD11b^+$ $Ly6c^+$ $Gr1^-$), KCs in the liver ($CD45^+$ $F4/80^+$), lineage $(Lin)^-$ cells in the bone marrow ($CD45^+$ $B220^-$ $Ly6g^-$ $CD11b^-$ $MRC1^-$), LSECs in the liver ($CD45^-$ $CD31^+$), proinflammatory TAMs ($CD11b^+$ $CD11c^+$ $Ly6c^+$ $F4/80^+$), protumoral TAMs ($CD11b^+$ $CD11c^-$ $Ly6c^-$ $F4/80^+$, $MRC1^+$), monocytes in the blood in Nude mice ($CD45^+$ $Ly6g^-$ $CD11b^+$ $MRC1^-$), monocytes in the blood ($CD45^+$ $CD11b^+$ $Gr1^-$), monocytes in the bone marrow ($CD45^+$ $CD11b^+$), monocytes in the liver ($CD45^+$ $CD11b^+$ $F4/80^-$ $CD11c^-$), monocytes in the lung ($CD45^+$ $Ly6g^-$ $CD11b^+$ $MRC1^-$), monocytes in the spleen ($CD45^+$ $Ly6g^-$ $CD11b^+$ $MRC1^-$), MRC1 macrophages in the spleen ($CD45^+$ $Ly6g^-$ $CD11b^-$ $MRC1^+$), MRC1 monocytes in the spleen ($CD45^+$ $Ly6g^-$ $CD11b^+$ $MRC1^+$), MRC1 macrophages in the spleen ($CD45^+$ $Ly6g^-$ $CD11b^-$ $MRC1^+$), MRC1 monocytes in the blood ($CD45^+$ $Ly6g^-$ $CD11b^+$ $MRC1^+$), MRC1 macrophages in the lung ($CD45^+$ $Ly6g^-$ $CD11b^+$ $MRC1^+$), neutrophils in the blood ($CD45^+$ $CD11b^+$ $Ly6c^+$ $Gr1^+$), parenchymal cells in the lung ($CD45^-$), parenchymal cells in the liver ($CD45^-$ $CD31/MRC1^-$), $Pentamer^+$ $CD8^+$ T cells in the tumor ($CD45^+$ $CD8^+$ $Pentamer^+$), resident monocytes in the blood ($CD45^+$ $CD11b^+$ $Ly6c^-$ $Gr1^-$), and T cells in the blood ($CD45^+$ $CD11b^-$ $CD3^+$). For FC analysis, we used the antibodies described in the key resources table.

Samples were acquired by using either a FACSCanto II or a FACSymphony™ A5 Cell Analyzer (BD Biosciences). For fluorescence activated cell sorting a BD FACSAria Fusion was used.

Mouse procedures

For endpoint analysis, mice were euthanized by cervical dislocation. The liver was perfused by injecting 10 mL of PBS containing 5 mM EDTA (Invitrogen) through the inferior vena cava and cutting the portal vein to allow exiting of the solution containing most circulating blood cells from the liver. When FC analysis but not immunofluorescence (IF) analysis was performed, 10 mL of IMDM (Corning) containing 0.35 mg/mL collagenase (Sigma-Aldrich) was injected through the inferior vena cava.

For systemic LV injection, LVs were diluted in PBS to obtain the desired TU to be injected per mouse in a volume ranging from 200 to 300 μL. For intravenous injection (i.v.), mice were warmed under an infrared/red-light lamp and the LVs were delivered in the tail vein. If not indicated otherwise, LVs were delivered 7 days after tumor placement. If not indicated differently, IFNα LV and Control LV were used at $5*10^9$ TU/kg; if not indicated differently, bidirectional LVs (*i.e.* miRT LVs), *Mrc1*.GFP LV and *Mrc1*.GFP.miRT LV were used at $1.5*10^{10}$ TU/kg. In experiments involving MC38.OVA cells, IFNα LV and Control LV were delivered 3 days after tumor engraftment at $1.5*10^{10}$ TU/kg. In all experiments untransduced (UT) mice were injected with PBS ranging from 200 to 300 μL.

Monoclonal antibody injection

Monoclonal antibodies were injected by an intraperitoneal injection in 100 μL diluted in PBS. The doses were: In-vivoMAB anti-mouse IL-10R (a-IL-10R, BioXCell, clone 1B1.3A) as well as the isotype control In-vivoMAB rat IgG1κ anti-horseradish peroxidase (IgG, BioXCell, clone HRPN) 1 mg/mouse in the first injection followed by injection of 0.5 mg/mouse every 4 days; In-vivoMAB anti-mouse CTLA-4 (a-CTLA-4, BioXCell, clone 9H10) and the isotype control In-vivoMAB polyclonal serum hamster (BioXCell) were injected at 0.1 mg/mouse 3 times per week; In-vivoMAB anti-mouse CD8a (a-CD8, BioXCell, clone 53-6.7) and the isotype control In-vivoMAB anti-trinitrophenol (IgG, BioXCell, clone 2A3) were used at 0.1 mg/mouse 2 times per week, first injection performed the day prior to LV injection. Monoclonal antibody treatment regimens, unless stated otherwise, were started concomitantly with LV delivery.

Mouse experimental liver metastasis models

We delivered AKTPF organoids or AKTPF cells by intrasplenic injection. Briefly, mouse fur was removed at the left upper flank of the mice by shaving followed by application of hair removal cream (Balea). Immediately prior to surgery, mice were injected with 50 μL carprofen (2.5 mg/mL) for pain management. Isoflurane (Iso-Vet) at a concentration of 3 % in flow of oxygen at 1.5 L/min was used to anesthetize the mice during surgery. AKTPF cells were resuspended in 50 μL of either Matrigel (BD Biosciences) for the AKTPF organoids or Geltrex (Thermo Scientific) and carefully injected into the spleen using a precooled syringe. For the injection of AKTPF cells from organoids, the latter were split two days prior to the injection. AKTPF cells from organoids or from 2D cultured AKTPF cells were dissociated into single cells and 30,000 cells per mouse were injected. The peritoneum wall was sutured by using adsorbable stitches while the skin was closed by applying stainless steel wound clips. Following surgery, mice were subjected to antibiotic treatment for one week by adding Baytril (Bayer) at a concentration of 0.5 mg/mL to the drinking water. For intrahepatic transplantation of MC38 and K8484 cells, the fur in the abdominal area of the mice was removed as described above. Pain management, anesthesia and surgery procedures were conducted as above. Single cells were obtained from cultured cancer cells and washed in PBS. We then injected 500,000 cells for MC38-mCherry and MC38-OVA cells, and 100,000 cells for MC38 and K8484 cells. Cells were injected in 5 μL PBS preferentially in the left liver lobe. Following surgery, mice were given antibiotic therapy as described above. Liver metastasis growth was measured by using magnetic resonance imaging (MRI), as described below, or by tumor weight (*i.e.* by dissecting the liver metastasis upon experiment termination and measuring its weight in a 10 mg precision digital bench scale).

Magnetic resonance imaging analysis for liver metastasis volume assessment

A 7-Tesla preclinical scanner (Bruker, BioSpec 70/30 USR, Paravision 6.0.1), equipped with 450/675 mT/m gradients (slew-rate: 3400-4500T/m/s; rise-time 140 μs) and a circular polarized mouse body volume coil with an inner diameter of 40 mm was used. During acquisition, mice were kept in anesthesia by inhaling isoflurane (Iso-Vet) at a concentration of 3 % in flow of oxygen at 1.5 L/min under a dedicated temperature control apparatus to prevent hypothermia. The breathing rate and the body temperature were continuously monitored (SA Instruments, Inc., Stony Brook, NY, USA). To aid liver lesion visualization, we used a hepatocyte-specific contrast agent, the Gd-EOB-DTPA (Bayer Schering Pharma), at 0.05 μmol/g of body weight. Axial fat-saturated T2-weighted images (RARE-T2, Rapid Acquisition with Relaxation Enhancement, TR = 3000 ms, TE = 40 ms, voxel-size = 0.125 × 0.100 × 0.8 mm, averages = 4,) and axial fat-saturated T1-weighted sequences (RARE-T1: TR = 540 ms, TE = 7.2 ms, voxel size = 0.125 × 0.100 × 0.8 mm, averages = 4) were acquired during the hepatobiliary phase of Gd- EOB-DTPA enhancement (10 minutes after administration). Volume measurement was performed by using the Medical Image Processing, Analysis, and Visualization (MIPAV) software.

Subcutaneous injection of MC38 cells

One-million MC38 cells were injected subcutaneously into the flank of mice in a volume of 100 μL of PBS. Tumor growth was monitored by measuring the dimensions (larger diameter x and lower diameter y) of the subcutaneous lesions using a caliper. Tumor volume was calculated with the formula:

$$Volume = \frac{3}{4} * \pi * (0.5 * diameter(x))^2 * 0.5 * \frac{diameter(y)}{2}$$

Blood collection and analysis

Blood was withdrawn either from the tail vein or the retroorbital vein plexus. Hemocytometer analysis was performed on whole blood by using the ProCyte DXTM (IDEXX). For FC analysis, red blood cell lysis was performed using the Red Blood Cell Lysis Buffer Hybri-Max™ (Sigma). To retrieve absolute numbers of hematopoietic cell populations, the percentage of cells out of $CD45^+$ cells, identified by using FC, was multiplied by the absolute count of white blood cells detected by hemocytometer analysis. For the collection of plasma, blood collected in Microvette® (Sarstedt) tubes was centrifuged at 3,000 rpm for 10 minutes at room temperature and precipitated red and white blood cells were discarded. For the collection of blood serum, blood collected in a conventional Eppendorf tube was incubated at room temperature for 40 minutes, and then centrifuged at 3,000 rpm for 10 minutes at room temperature. The fraction of containing platelets, red and white blood cells was discarded. Quantification of IFNα content in the blood was performed on plasma using the Mouse IFN Alpha All Subtypes ELISA KIT High Sensitivity (pbl Assay Science) according to manufacturer's instruction. For assessment of transaminases in the serum, ALT (Instrumentation Laboratory) and AST (Instrumentation Laboratory) quantification kits were used with an International Federation of Clinical Chemistry and Laboratory Medicine–optimized kinetic ultraviolet (UV) method in an ILab Aries chemical analyzer (Instrumentation Laboratory). In parallel, SeraChem Control Level 1 and Level 2

(#0018162412 and #0018162512) were analyzed as quality control. The quantification of autoreactive antibodies was performed on blood serum. Autoantigen microarrays were manufactured in the Microarray & Immune Phenotyping core Facility of University of Texas Southwestern Medical Center, Dallas, TX, USA. A selection of 120 autoantigens was made based on published literature, prior known autoantibodies in various immune related disease, cancer, allergic disease etc. 8 positive control proteins (Ig control 1:2, Ig control 1:4, Ig control 1:8, Ig control 1:16, anti-Ig control 1:2, anti-Ig control 1:4, anti-Ig control 1:8, anti-Ig control 1:16) were also imprinted on the arrays as positive controls. Mouse serum samples were first treated with DNAse I to remove free-DNA and then applied onto autoantigen arrays with 1:50 dilution. The autoantibodies binding to the antigens on the array was detected with cy3-labeled anti-mouse IgG and cy5-labeled anti-mouse IgM, and the array slides were scanned with Genepix 4400A scanner with laser wavelengths 532nm for cy3 and 635nm for cy5 to generate Tiff images. Genepix Pro 7.0 software is used to analyze the images and generate the genepix report (GPR) files (Molecular Devices, Sunnyvale, California, USA). The net fluorescent intensity (NFI) of each antigen was generated by subtracting the local background and negative control (Phosphate buffered saline or simplified as PBS) signal. The NFI were normalized by the absolute amount of IgGs detected in each sample (based on the 1:2 anti-Ig control). Then we normalized each individual value by the average detected across all experimental mice included in this study (excluding the positive control) resulting in a value describing the fold change compared to the average.

Processing of organs for FC analysis

For FC analysis, organs were cut into small pieces and incubated with a tissue digestion solution composed of 1 mL IMDM (Corning) supplemented with 0.35 mg/mL collagenase type IV (from *Clostridium histolyticum*, Sigma-Aldrich), 1 mg/ml dispase II (Gibco) and 0.2 mg/ml DNAse (Roche) were added. Tissue digestion solution was then incubated at 37 °C under agitation at 350 rpm for 10 min. The tissue was then further dissociated by pipetting and filtered using 0.4 μm cell strainers (Corning).

Processing of organs for imaging

For IF, tissues were incubated in a paraformaldehyde solution 4 % in PBS (PFA; ChemCruz®) for 4-12 hours (according to tissue size) at 4 °C. Afterwards, the PFA was exchanged for a solution of 10% sucrose (Sigma-Aldrich) and 0.02% NaN3 in H2O. After 8 - 15 h incubation at room temperature, sucrose solution was increased to 20%, and to 30% after additional 8 - 15 h. The organ was then embedded into Killik, O.C.T. Compound embedding medium for cryostat (Bio-Optica). Sections of 20 mm thickness were prepared and placed on glass slides using a cryostat. Sections were dried for 30 minutes at room temperature. For antigen retrieval, slides were incubated for 20 minutes in a 95 °C preheated water bath in the following solutions: (1) low pH antigen retrieval: 10 mM citric acid in H2O, pH adjusted to pH 6; (2) high pH antigen retrieval: 10 mM Tris base and 1mM EDTA plus 0.05 % tween in H2O, pH adjusted to pH 9. Slides were then cooled down in the indicated solution for 15 minutes at room temperature and then slides were washed with PBS 3 times. Blocking was performed by using a blocking buffer composed of 5 % normal donkey serum, 1 % BSA (Sigma-Aldrich) and 0.3 % TritonTM X-100 (Sigma) in PBS. For staining with mouse primary antibodies, mouse on mouse IgG blocking solution (Vector Laboratories) was added to the blocking buffer according to manufacturer's instruction. After 1h of blocking at RT, the blocking buffer was replaced by blocking buffer containing the indicated concentrations of primary antibodies and incubated overnight at 4 °C. The sections were then washed with washing buffer (PBS containing 0.3 % TritonTM X-100) for 5 times. Sections were stained with the secondary antibodies in blocking buffer at the indicated concentrations. An incubation for 1 h at room temperature in the dark was performed followed by 6 washing steps with washing buffer. For staining of the nuclei, sections were covered with a 1/2000 dilution of Hoechst 33342 solution (life technolog) in PBS for 2 min. Slides were washed additional 3 times with PBS and mounted using Fluoromount-G® (SouthernBiotech). Images were acquired using an SP8 lightning confocal microscope (Leica Microsystems).

For the histopathologic evaluation of side effects, the indicated organs were collected from mice after euthanasia and fixed in 10% buffered formalin, embedded in paraffin wax, sectioned at 3 μm, and stained with haematoxylin and eosin (H&E) following OECD Good Laboratory Practices principles, principles of data integrity and applicable GLP SR-TIGET SOPs. Histopathological changes were evaluated by an experienced pathologist and graded on a scale of 1 to 5 as minimal (1), mild (2), moderate (3), marked (4), or severe (5); minimal referred to the least extent discernible and severe the greatest extent possible. Slides were digitalized with scanner Leika Aperio Scanscope XT at 200x magnification and reviewed by an expert pathologist.

IF analysis of human livers containing CRC-liver metastases was performed on formalin-fixed and paraffin-embedded (FFPE) tumor specimens with antibodies described in the key resources table. Representative images were captured with a Nikon 80i Eclipse fluorescence microscope at a 500x – 1000x magnification. Quantification was performed by expert pathologist, at least 200 $CD4^+$ cells were enumerated in peritumoral area (liver/metastasis interface) and in intra metastatic tumor stroma and the percentage of double positive $LAG3^+$ $CD4^+$ or $CTLA\text{-}4^+$ $CD4^+$ out of $CD4^+$ cells were measured. Secondary sample staining of human samples was performed by employing the Automated Discovery Ultra IHC/ISH research platform (Roche).

For preparation of H&E staining of human and murine livers containing metastases, samples were fixed in 10% buffered formalin, embedded in paraffin wax, sectioned, and stained with H&E. Slides were analyzed by an experienced pathologist and were digitalized with scanner Leika Aperio Scanscope XT at 200x magnification.

Single-cell RNA (scRNA) sequencing

Immediately after perfusing the livers, liver metastases were isolated and dissociated into single cells as described above. Single cells were resuspended in MACS buffer containing 7AAD (BioLegend). Viable cells were sorted by gating on 7AAD negative cells. Sorted cells were further processed for scRNA sequencing. ScRNA sequencing was performed using the Next GEM Single Cell

3' GEM Kit v3.1 from Chromium 10X according to manufacturer's recommendation (User Guide Chromium Next GEM Single Cell 3' Reagent Kits v3.1). We loaded 10,000 cells belonging to the same sample per reaction. We sequenced 8 samples, 100 bp paired-end reads in a NovaSeq 6000 Illumina apparatus, $4.75*10^9$ reads total. Base call files obtained as result from the Illumina sequencing were converted into FASTQ files and processed with the *Cell Ranger* Single-Cell Software Suite (10X Chromium v3.1.0) using default setting. In detail, the demultiplexed samples were aligned against the murine mm10 reference genome employing the STAR aligner (producing alignment files in BAM format) and a UMI-count gene quantification was performed (based on the reference annotation). This latter gene-by-cell matrix was then imported into R and processed with the Seurat package (http://satijalab.org/seurat v4.0.3). As a first step of the analyses, doublets were assessed using the DoubletFinder (v3) software. More precisely, following the 'Best-Practices' suggested by the authors for scRNA-seq processing, the following parameters were selected to annotate doublets in each sample:

Parameters used for the DoubletFinder v3.

Sample	Treatment cohort	nExp	pK
Sample 3	Control	0.07	0.005
Sample 4	Resistant	0.09	0.005
Sample 7	Control	0.07	0.005
Sample 10	Partial Responder	0.09	0.01
Sample 11	Partial Responder	0.07	0.005
Sample 14	Resistant	0.09	0.005
Sample 19	Control	0.05	0.005
Sample 22	Partial Responder	0.09	0.2
GG-11	Control LV	0.05	0.05
GG-18	IFNα LV	0.07	0.2
GG-22	IFNα LV + a-CTLA-4	0.09	0.005
GG-23	IFNα LV	0.07	0.03
GG-25	Control LV	0.07	0.03

Samples were merged into a single Seurat dataset, using Seurat package (http://satijalab.org/seurat v4.0.3), keeping the information about the original sample as well as the corresponding treatment cohort. Then, the pre-processing step on the produced data started by removing cells with a low sequencing quality, those with a feature count below 1,000 and above 6,000, as well as cells with a fraction of mitochondrial genes higher than 10 %. Afterwards, cells annotated as doublets with the DoubletFinder (v3) were excluded from the analysis with Seurat. RNA UMI-counts were normalized using a global-scaling normalization method and the Variance Stabilizing Transformations (SCTransform) was performed to scale based on the percentage of mitochondrial genes, the absolute count of RNAs in each cell, and the difference between S and G2/M cell cycle scores computed for each cell. A principal component analysis with 50 principal components (PCs) was performed for dimensional reduction, and a UMAP-representation as well as clusters (with a resolution of 1.2) were computed on those reductions. Marker genes for each cluster were obtained using the *FindAllMarkers* Seurat function, and consequently clusters were annotated and manually curated, including a small population of undefined cells which was then removed from the dataset. Analysis of the subclusters "T and NK cells" and "APCs" was performed accordingly. First, T and NK cells were isolated using the subset function, then SCTransform based on the RNA-count matrix was performed, followed by a principal component analysis with 35 PCs, and cluster identification with a resolution of 0.8. At this resolution, $CD4^+$ T cells, $CD8^+$ T cells, γδ T cells, NK cells, ILCs and NKT cells were identified, as well as a population of undefined cells. $CD4^+$, $CD8^+$ and NKT cells were further refined by a sub-clustering. The number of PCs used for sub-clustering in NKT cells, $CD8^+$ T cells and $CD4^+$ T cells were 30, 35, and 35, while the resolution was 0.6, 0.3 and 0.3, respectively. Similarly, a specific analysis was performed in the APC compartment with 35 PCs and a resolution of 1.2. Cluster annotations were reintegrated into the full dataset and undefined cells were removed. SCTransform was repeated on the RNA slot and PC analysis was repeated on the full dataset as well as the subsets T and NK cells and APCs with the same parameters depicted before. Batch removal with harmony (on the sample origin) was performed on the subset of TAMs, IFNα TAMs, and KCs to better assess their composition. Top upregulated markers of each population were calculated based on the *FindAllMarkers* function and a heatmap was generated based on the top 20 upregulated genes in each cluster to represent them. For the calculation of differentially expressed genes within individual clusters comparing the different treatment cohorts, namely control, partial responders and resistant, the *FindMarker* function was utilized. For GSEA the gene sets from https://www.gsea-msigdb.org/gsea/msigdb/genesets.jsp were used. For the gene sets extracted from Cilenti et al.,[56] the genes upregulated in BMDMs stimulated with the indicated cytokine *in vitro* compared to unstimulated BMDMs were included in the gene set term. Furthermore, the $CD8^+$ T cell exhaustion signature, termed Exhaution_T_cells (Wherry et al.,) was retrieved from a previous publication.[57] Only GO terms containing a minimum of 7 and maximum of 500 overlapping genes between the GO term and genes in the data set were considered in the analysis.

The scRNA + TCR sequencing was performed accordingly using Next GEM Single Cell 5′ GEM Kit v2 in combination with the Single Cell Mouse TCR Amplification Kit and we sequenced the GEX at $2.45*10^8$ reads per sample and the TCR libraries at $2*10^7$ reads per sample of 5 samples at a dual index 100 bp paired-end configuration in a NovaSeq 6000 Illumina apparatus. The downstream analysis was performed as described above. Cluster annotation was performed manually as described previously. No SCT transformation was performed following the removal of undefined cells. TCR analysis was performed with the R/Bioconductor package scRepertoire to identify clonotypes in each sample and computing their frequency (considering the the amino acid sequence of the CDR3 region of the beta chain). TCR clonotypes were classified as unique (1 cell containing a specific TCR clone), small (2 to 5 cells containing the same TCR), medium (6 to 15 cells containing the same TCR), large (16 to 25 cells containing the same TCR) and hyperexpanded (more than 25 cells containing the same TCR), according to their numerosity. Codes and data for scRNA sequencing analysis are available at http://www.bioinfotiget.it/gitlab/custom/squadrito_livertumor2022 and at NCBI's Gene Expression Omnibus GEO:GSE221360 respectively.

Spatial transcriptomic analysis

Immediately after perfusion of the liver, small pieces of the liver containing metastasis were shock-frozen in isopentane. Afterwards, the samples were embedded in Killik, O.C.T. Compound embedding medium for cryostat (Bio-Optica). To process the samples for Visium analysis, 10 μm sections were prepared using a cryostat and placed on the Visium slides. For that purpose, the cryostat was cooled to –16 °C. Methanol fixation and H&E staining was performed according to the manual provided by 10x Genomics under the name Methanol Fixation, H&E Staining & Imaging for Visium Spatial Protocols (10x Genomics) using a Aperio ePathology digital scanner (Leica Biosystems) for image acquisition. We performed spatial transcriptomics on 36 mm^2 sections of liver containing metastatic lesions. The samples were processed for Visium analysis according to manufacturer's instructions (10X Genomics). We sequenced 8 samples, 100 bp paired-end sequencing in a NovaSeq 6000 Illumina apparatus, $1.5*10^9$ reads total. Illumina results were analyzed by using the *Space Ranger* software v1.2.2. More precisely, samples were demultiplexed using the *mkfastq* utility (which exploits the Illumina's *bcl2fastq* program) to produce initial FASTQ files. Then, starting from these latter input reads and the corresponding microscope slide image, the *count* step was run on each sample to perform alignment (exploiting STAR), tissue detection, fiducial detection, and barcode/UMI counting. This results in a spot-by-gene matrix, which was imported (with the corresponding tissue slide image) and analyzed with Seurat. For all samples separately a SCTransform and normalization was performed, and variable features were determined. Sample data were integrated into one object by applying the *IntegrateData* function, in which the anchor set was previously determined by using the *FindIntegrationAnchors* function with anchor features being defined by the *SelectIntegrationFeatures* function. Data scaling was performed on the whole dataset followed by a principal component analysis. For the generation of a UMAP plots containing cluster determination, 25 PCs were employed and a resolution of 0.1 was used. Clusters were further manually merged towards the 8 clusters based on their marker genes. Differentially expressed genes in each cluster were determined using the *FindMarker* function. Individual spots belonging to clusters 1 and 6 were annotated as tumor, while all the remaining ones as liver. Based on a moving average function, spots annotated as liver and tumor were divided into four zones each, leading to a classification of each spot dependent on the distance to the tumor-liver interface. For that purpose, the geographic spot matrix was converted to a binary form based on tumor and liver annotations. To define the closeness to the tumor-liver interface, the moving average for each spot assigned as tumor and liver was determined separately for the tumor and liver area with the function *ma.matrix* (package OLIN) using the following formular:

$$moving\ average\ =\ ma.matrix[\text{delta}\ =\ 3] + 2 * ma.matrix[\text{delta}\ =\ 2]$$

For the determination of the zones, the following thresholds were set: zone A: moving average (tumor) > 2.96; zone B: moving average (tumor) $\leq$ 2.96 and > 2.7; zone C: moving average (tumor) $\leq$ 2.7 and > 2.3; zone D: moving average (tumor) $\leq$ 2.3; zone E: moving average (liver) $\leq$ 1.7; zone F: moving average (liver) $\leq$ 1.91 and > 1.7; zone G: moving average (liver) $\leq$ 2.095 and > 1.91; zone H: moving average (liver) > 2.095. Differentially expressed genes comparing the different zones in the different treatment cohorts were calculated using the *FindMarker* function. GSEA determination was performed as described for scRNA sequencing as described above.

Signatures derived from the scRNA sequencing experiment described above as well as established signatures (Table S6) were used to better dissect the spots within the computed zones and characterize them. In details, the average expression of each signature was computed by using the *AddModuleScore* function of Seurat, and then the median value for each zone was calculated.

Codes and data for spatial transcriptomics analysis are available at http://www.bioinfotiget.it/gitlab/custom/squadrito_livertumor2022 and at NCBI's Gene Expression Omnibus https://www.ncbi.nlm.nih.gov/geo/query/acc.cgi?acc=GSE221360 respectively.

Bulk RNA sequencing of samples from human liver metastases

Total RNA was extracted from OCT-embedded samples of CRC liver metastases using AllPrep DNA/RNA Mini kit (Qiagen). RNA samples were quantified with Qubit RNA HS Assay (Life Technologies) and their integrity was assessed using High Sensitivity RNA ScreenTape Assay on 4200 TapeStation System (Agilent Technologies). Libraries were prepared using TruSeq Stranded mRNA kit (Illumina) and then sequenced 1x100bp on the Illumina NovaSeq 6000 platform. Reads were trimmed using Trimmomatic, version 0.32, in order to remove adapters and to exclude low-quality reads from the analysis. The remaining reads were then aligned to the reference human genome hg38, Gencode version 31, using the STAR aligner, version 2.5.3a. The FeatureCounts tool was used to assign exonic reads to the corresponding genes. Expression data were imported in the R statistical environment (R version 3.1.1) to

be analysed. Only genes showing a counts per million (CPM) value higher than 1 in at least one sample were defined as expressed and used for the analysis. Data were shown as reads per kilobase of transcript per Million reads mapped (RPKM) and log2-transformed. The gene signatures score for TR1-up and IFNα (Table S3) were evaluated: for each sample, the scores of the considered signatures were defined as the average expression of the corresponding genes. Pairwise correlations of the signatures were calculated using the Pearson's index. Correlations between individual genes were also assessed. Moreover, linear regressions were fitted to describe the relationship between each pair of signatures.

The sequencing data have been deposited at NCBI's Gene Expression Omnibus repository and are accessible through accession number GSE200133 and in a previous study.[58]

Nanostring analysis on patient metastases

Total RNA was extracted from a total of 15 formalin-fixed paraffin-embedded samples, from both tumor and peritumor area, using the Maxwell® RSC RNA FFPE Kit (Promega Corporation) following manufacturer's instructions. Total RNA was quantified using the Qubit RNA HS Assay Kit on Qubit 3.0 Fluorometer (ThermoFisher Scientific).

Gene expression analysis was performed using the NanoString nCounter® PanCancer IO 360™ Panel, which analyzes 770 genes involved in the interplay between cancer cells and the TME. Briefly, 50-300 ng of total RNA were hybridized to Nanostring probes for 16 hours at 65°C. The hybridized probes were purified and counted using the nCounter Prep Station following manufacturer's instructions. Counts of fluorescent barcodes were obtained using the Digital Analyzer at 280 fields of view (FOV).

Raw data generated by Nanostring were analysed by employing R. Gene expression data were normalized using quantile normalization. The Tr1 signature score and IFNα signature score describe the geometric mean of the normalized expression of the genes within the respective gene set (as shown in Table S3). The rho coefficient was calculated by using spearman correlation between the expression level of the indicated gene and the genes in the IFNα signature within each patient. Otherwise, rho coefficient were calculated among all patients between the expression level of each gene in the IFNα signature score and any other gene excluding those present in the IFNα signature.

Statistical methods

Comparisons between two independent groups were performed with Mann-Whitney test and, when needed, p-values were adjusted for multiple testing with Bonferroni's correction. Comparisons between paired groups were performed, in general, with the paired Wilcoxon test. Since for n = 5, the minimum achievable two-sided p-value of the test is 0.0625, a corresponding nonparametric test based on bootstrap sampling was employed for that sample size (function boot.t.test in the MKinfer R package). When comparing more than two groups with the aim of performing all pairwise comparisons, Kruskal-Wallis test was employed followed by post-hoc analysis through Dunn's test and p-values adjusted with Bonferroni's correction. Instead, when the aim was comparing only prespecified pairs of groups, the Mann-Whitney test was used and p-values were adjusted with Bonferroni's correction. In case it was necessary to account in the analysis for the order of the mice in the experiment, the comparison among groups was performed with a linear model (ANCOVA). The terms of the model corresponded to the groups and to a variable representing the order in which the mice were taken. The response variable was transformed by using the transformation log(x+0.01) in order to meet the normality assumptions of the model. The correlation among two variables was performed with Spearman's correlation coefficient.

In all analyses, the significant level was set at 0.05. All statistical analyses were performed using R 3.6.2 (http://www.R-project.org/).

Figures were created using Prism 9 Version 9.3.1.

FC analyses were performed using FlowJo version 10.8.1 or FCS Express Version 7.12.0007.